Economic Geology, v. XXX, no. XX, pp. X–X

# Rhenium Enrichment in the Muratdere Cu-Mo (Au-Re) Porphyry Deposit, Turkey: Evidence from Stable Isotope Analyses ($\delta^{34}S$, $\delta^{18}O$, $\delta D$) and Laser Ablation-Inductively Coupled Plasma-Mass Spectrometry Analysis of Sulfides

Katie McFall,[1,2,†] Stephen Roberts,[1] Iain McDonald,[2] Adrian J. Boyce,[3] Jonathan Naden,[4] and Damon Teagle[1]

[1]*Ocean and Earth Science, National Oceanography Centre Southampton, University of Southampton, European Way, Southampton SO14 3ZH, United Kingdom*

[2]*Cardiff University School of Earth and Ocean Sciences, Main Building, Park Place, Cardiff CF10 3AT, United Kingdom*

[3]*Scottish Universities Environmental Research Centre (SUERC), Scottish Enterprise Technology Park, Rankine Avenue, Glasgow G75 0QF, United Kingdom*

[4]*British Geological Survey (BGS), Nicker Hill, Keyworth, Nottingham NG12 5GG, United Kingdom*

## Abstract

The Muratdere Cu-Mo (Au) porphyry deposit in western Turkey contains elevated levels of rhenium and is hosted within granodioritic intrusions into an ophiolitic mélange sequence in the Anatolian belt. The deposit contains several stages of mineralization: early microfracture-hosted molybdenite and chalcopyrite, followed by a quartz-pyrite-chalcopyrite vein set associated with Cu-Au grade, a quartz-chalcopyrite-pyrite-molybdenite vein set associated with Cu-Mo-Re grade, and a later polymetallic quartz-barite-sphalerite-galena-pyrite vein set. The rhenium in Muratdere is hosted within two generations of molybdenite: early microfracture-hosted molybdenite and later vein-hosted molybdenite. In situ laser ablation-inductively coupled plasma-mass spectrometry analysis of sulfides shows that the later molybdenite has significantly higher concentrations of Re (average 1,124 ppm, $\sigma$ = 730 ppm, n = 43) than the early microfracture-hosted molybdenite (average 566 ppm, $\sigma$ = 423 ppm, n = 28). Pyrite crystals associated with the Re-rich molybdenite have higher Co and As concentrations than those in other vein sets, with Au associated with As. The microfracture-hosted sulfides have $\delta^{34}S$ values between −2.2‰ and +4.6‰, consistent with a magmatic source. The vein-hosted sulfides associated with the high-Re molybdenite have a $\delta^{34}S$ signature of 5.6‰ to 8.8‰, similar to values found in peridotite lenses in the Anatolian belt. The later enrichment in Re and $\delta^{34}S$-enriched S may be sourced from the surrounding ophiolitic country rock or may be the result of changing redox conditions during deposit formation.

## Introduction

Porphyry Cu deposits provide 90% of the world's rhenium production (Sinclair, 2007; Polyak, 2016). Rhenium is an essential element in a number of industrial applications, including superalloy production to make Ni-Re alloys for use in turbine blades for jet and industrial gas turbine engines and Pt-Re catalysts that improve the efficiency of crude oil refining (John, 2015). The relative restriction of supply of Re and the lack of viable alternative elements for its industrial uses has led to Re being classified as a "critical metal" by the United Kingdom and Russia (Chakhmouradian et al., 2015).

The Muratdere Cu-Mo (Au-Re) porphyry deposit, located in the Tethyan metallogenic belt, Turkey, has a Joint Ore Reserves Committee (JORC)-compliant inferred resource of 51 million tonnes, including 186,000 tonnes Cu, 204,296 oz Au, 3.9 million oz Ag, 6,390 tonnes Mo, and 17,594 kg Re (Stratex International, 2017), with whole-rock Re concentrations of up to 2.37 ppm. Muratdere is considerably enriched in Re when compared with average Re concentrations of andesite at 0.2 to 0.6 ppm and granodiorite at 0.02 to 0.09 ppm (Imai et al., 1995), and an average crustal Re concentration of 0.7 ppb (Naumov, 2007). Rhenium in porphyry deposits is typically hosted in molybdenite ($MoS_2$) (Fleischer, 1959) with average concentrations of Re in molybdenite between 0.5 and >5,000 ppm in global porphyry deposits (Mao et al., 2003; Berzina et al., 2005; Voudouris et al., 2009). Despite our understanding that the Re in porphyry systems is located within molybdenite (Fleischer, 1959), the mechanisms of Re enrichment in porphyry Cu deposits remain poorly understood. These uncertainties include the source and mechanisms of Re enrichment in porphyry deposits, the mechanisms of its incorporation into molybdenite, and why some systems are Re enriched whereas others are not.

This paper provides the first account of the geologic and mineralogical features of porphyry Cu-Mo (Re-Au) mineralization at Muratdere. The study integrates data generated by X-ray diffraction (XRD), electron probe microanalysis (EPMA), scanning electron microscope (SEM), stable isotope (H, O, S), and laser ablation-inductively coupled plasma-mass spectrometry (LA-ICP-MS) analyses of molybdenite and pyrite samples to provide insights into trace element enrichment in sulfides in porphyry Cu deposits and the source and mechanisms of Re enrichment in the Muratdere deposit.

### *Current models for rhenium enrichment in porphyry Cu deposits*

Re is a moderately chalcophile metal that mimics the behavior of Cu and the platinum group elements (PGEs) in melts, preferentially partitioning into sulfide droplets in hot mafic melts (Patten et al., 2013). However, Re compatibility also has a

† Corresponding author: e-mail, mcfallk@cardiff.ac.uk



ISSN 0361-0128; doi: 10.5382/econgeo.4638; 24 p.
Digital appendices are available in the online Supplements section.



Published online: April 29, 2019

strong dependency on $f_{O_2}$, behaving as a chalcophile element in relatively reduced magmas but preferentially partitioning into silicate minerals in more oxidized arc magmas (Fonseca et al., 2007).

One suggested source of Re in porphyry deposits is ultramafic melts that rise through the crust and are injected into colder, felsic porphyry-related magma, enriching it in sulfur, Au, and Re, along with other volatiles and chalcophile elements (Hattori and Keith, 2001; Sinclair and Jonasson, 2014). This hypothesis is supported by a number of observations, including the positive correlation between Re and Au contents of porphyry deposits globally (Sinclair and Jonasson, 2014); rare earth element patterns consistent with amphibole and residual garnet fractionation in igneous rocks associated with porphyry deposits (Richards, 2011); and the common association of Re- and Au-enriched porphyry deposits with mafic magmatic and volcanic phases. Porphyry deposits believed to involve mantle underplating or metasomatism, or the melting of mafic or ultramafic rocks as part of their genesis also tend to have higher Re in molybdenite than those hosted by intermediate crustal rocks (Stein et al., 2001a; Berzina et al., 2005). An additional potential source of Re is the subduction of anoxic sediments, which carry high Re concentrations (Sun et al., 2003), and there are many reports of molybdenite samples with high Re contents at convergent margin volcanoes, with concentrations of up to 11.5 wt % Re in molybdenite (Bernard et al., 1990).

Comparing the Re content of molybdenite samples from more than 75 porphyry deposits, Berzina et al. (2005) concluded that bulk Re concentrations are closely linked to the parent magmas, with Re deposition controlled by the solubility of Re-hosting phases in the hydrothermal fluid. Rhenium is transported as a chloride complex in supercritical hydrothermal fluids (Xiong and Wood, 2002; Xiong et al., 2006); however, the hydrothermal mobility of Re is affected by fluid temperature, pH, and $f_{O_2}$. Berzina et al. (2005) note that deposits formed under oxidizing conditions contain more Re, as is the case for deposits that display evidence from biotite and apatite compositions of elevated $f_{Cl}$ and $f_F$ in the hydrothermal fluids (Berzina et al., 2005). In addition, deposits with high Re contents in Siberia have low initial $^{87}Sr/^{86}Sr$ values (0.70406–0.70496), whereas low-Re deposits have higher $^{87}Sr/^{86}Sr$ values, possibly reflecting crustal contamination. They also note that most Re-bearing parent magmas have $\delta^{34}S_{\text{Canyon Diablo Troilite (CDT)}}$ values of about 0‰, as expected for a magmatic sulfur source (Berzina et al., 2005).

Paradoxically, although Re is most commonly hosted by molybdenite in porphyry deposits, Mo-dominated (Mo-Cu) porphyry deposits typically contain less Re than Cu-dominated (Cu-Mo or Cu-Au-Mo) deposits. The Re content of global porphyry deposits appears to increase with increasing Cu/Mo ratio (Berzina et al., 2005). This has been attributed to the fact that the Re budget available in the source melt is preferentially sequestered by molybdenite. Assuming all available Re is taken up by the molybdenite present, the limited presence of molybdenite in low-molybdenum deposits results in higher Re concentrations in molybdenite crystals, whereas in high-molybdenum deposits the Re content is diluted across many more molybdenite crystals (Stein et al., 2001b).

The Muratdere deposit was chosen for study because it has relatively high Re concentrations compared with Cu-Mo porphyry deposits globally (Berzina et al., 2005) and contains two generations of molybdenite with different Re contents, which allows a study of the processes of Re incorporation into molybdenite. In addition, the presence of ophiolite country rock, including peridotites, allows us to test whether a metal-enriched country rock can enhance porphyry deposit metal endowment.

## Regional Geology

The Muratdere Cu-Mo porphyry deposit is situated near Bozüyük in the Bilecik Province in western Turkey and is within the Tethyan metallogenic belt (Yigit, 2006). In Turkey, the porphyry deposits in the Tethyan belt are related to Late Cretaceous to Miocene granitoids formed in association with the closure of the Neotethys and the Paleotethys (Yigit, 2006, 2009) and are associated with a number of island arcs and continental fragments (Richards, 2014). Following the closure of the Paleotethys Ocean in the Early Jurassic, northward subduction of the Neotethys caused calc-alkaline magmatism and ophiolite accretion through to the Late Cretaceous (Boztug and Arehart, 2007; Kaygusuz et al., 2008; Dokuz et al., 2010), although the majority of the volcanic and magmatic products from that period have since been eroded away. The Muratdere deposit is situated 250 km west of Ankara in the North Anatolian belt, a Jurassic-Cretaceous ophiolitic mélange which stretches across the center of Turkey (Tekeli, 1981; Fig. 1A). The deposit is approximately 30 km to the south of the Izmir-Ankara-Erzincan suture zone, a feature that was formed in the Late Cretaceous to Paleocene as the Kirşehir microcontinental block collided with the Central Pontide margin (Kaymakci et al., 2009; Robertson et al., 2009; Sarıfakıoğlu et al., 2010; Lefebvre et al., 2013; Espurt et al., 2014). As subduction of the Neotethys continued through the late Paleocene to early Eocene, the Tauride-Anatolian block collided with the Izmir-Ankara-Erzincan suture zone (Kaymakci et al., 2009; Arslan et al., 2013). This collision led to calc-alkaline magmatism in response to slab rollback and breakoff (Boztuğ et al., 2006; Boztug and Arehart, 2007; Boztuğ and Harlavan, 2008; Kaygusuz et al., 2008), and this postcollisional magmatism is associated with many porphyry deposits across the north of Turkey, including Muratdere. This magmatism is thought to be particularly metal endowed due to upwelling of asthenospheric mantle during postcollisional extension, which caused partial melting of lithosphere previously modified by subduction (Altunkaynak and Dilek, 2006; Altunkaynak, 2007; Akay, 2009; Sarıfakıoğlu et al., 2013; Kuscu, 2016).

The Muratdere deposit lies within the Tavşanli zone, south of the Izmir-Ankara-Erzincan suture zone, a blueschist sequence overlain by a Late Cretaceous accretionary complex (Okay, 2008; Fig. 1B). Ophiolite nappes are present along the Izmir-Ankara-Erzincan suture zone, preserving mafic-ultramafic rocks that are remnants of oceanic lithosphere, and an ophiolitic mélange, which comprises oceanic and continental fragments (Uysal et al., 2009). Muratdere is hosted by granodioritic bodies that intruded into an extension of the Dağküplü ophiolite, within the Eskişehir ophiolite group (Uysal et al., 2009; Sarıfakıoğlu et al., 2010), a 1,500- to 4,500-m-thick sequence of dismembered peridotite tectonite and mafic cumulates, comprising an incomplete and inverted ophiolite sequence (Uysal et al., 2009). The Dağküplü section

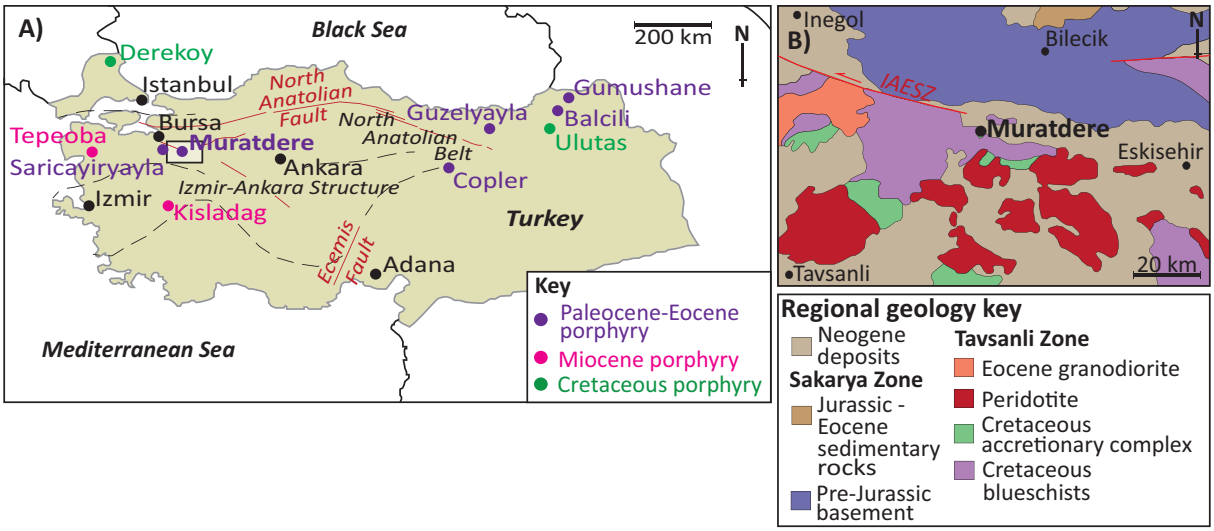


Fig. 1. A) Generalized map of Turkey, highlighting local deposits and regional structural features. B) Map showing the regional geology of the area around Muratdere (after Okay and Tüysüz, 1999), outlined in (A) by the black rectangle. IAESZ = Izmir-Ankara-Erzincan suture zone.

includes mantle peridotite, gabbroic cumulates, diabase dikes, and amphibolite facies metamorphic sole rocks (Okay, 2008; Sarıfakıoğlu et al., 2010).

These ophiolitic units were intruded by a 400-km-long and 60-km-wide, E-W–trending belt of Eocene granitoids (48–54 Ma; Fig. 1B, Harris et al., 1986; Ataman, 1972; Bingöl et al., 1982; Delaloye and Bingol, 2000; Altunkaynak, 2007; Okay, 2008). The granitoids range in composition from diorite and granodiorite to syenite. The volcanic equivalents are not preserved in the area. The plutons are commonly associated with granodiorite porphyry sheets with compositional zoning from core to edge (Altunkaynak, 2007; Okay, 2008). The early Eocene magmatism in this region is interpreted to be the result of extension, following the exhumation of thickened crust after final suturing of the Eurasian and Afro-Arabian plates at ~52 Ma (Kuscu, 2016).

## Deposit Geology

The Muratdere Cu-Mo deposit is hosted by a suite of E-W–striking granodioritic intrusions, over a strike length of 4 km

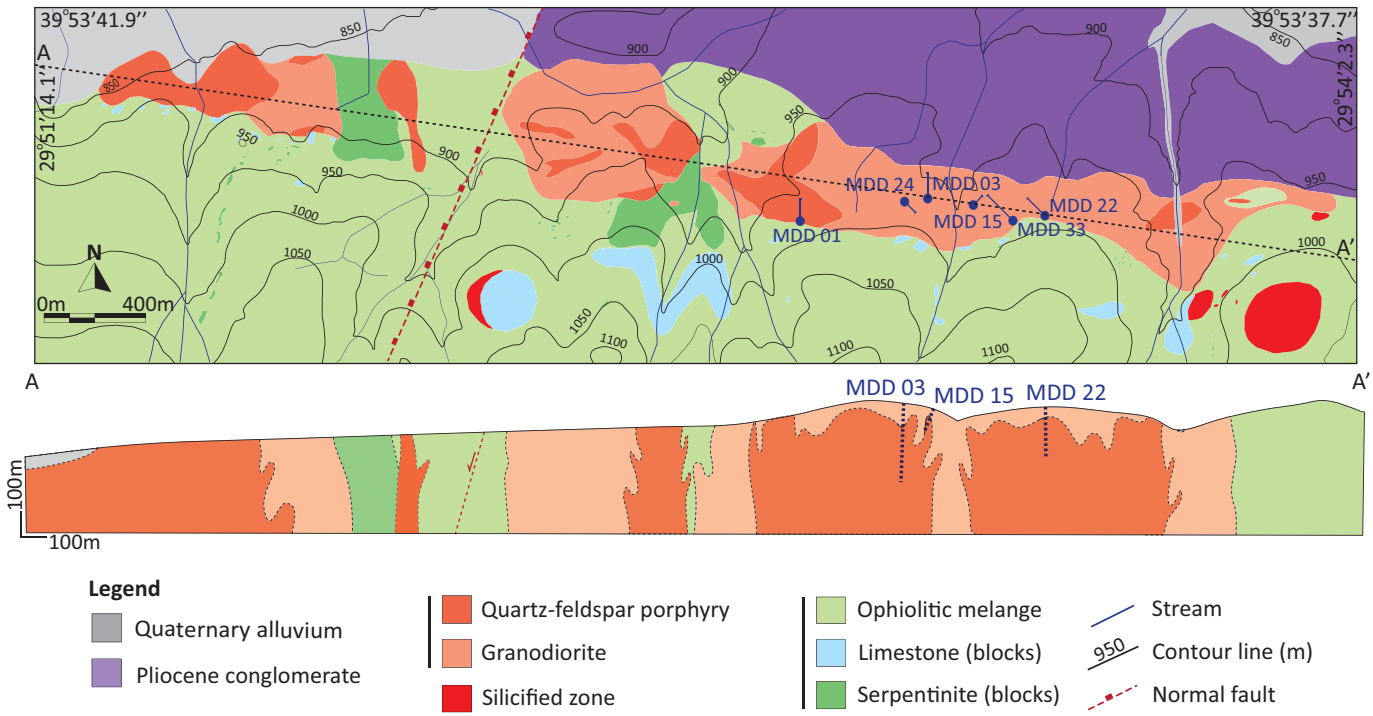


Fig. 2. Geologic map and cross section of the Muratdere deposit, showing drill hole locations. Interpretive cross section drawn from logging performed during this project and company data provided by Stratex International.

and an average width of 400 m (Fig. 2). The exact age of the plutons is not known, but they are inferred to be Eocene due to their petrological similarity and spatial correlation with other E-W–trending granitoids in the region (Altunkaynak, 2007; Yigit, 2009). The intrusions are hosted within an ophiolitic mélange, which comprises peridotite lenses, gabbro dikes, gabbro cumulates, and limestone blocks, all of which have been metamorphosed to greenschist facies. Highly serpentinized peridotite is observed at the bottom of one of the drill holes (MDD 03 from 283 m; Fig. 3).

The deposit is situated within the Thrace-Eskişehir fault zone, an NW-SE–trending active dextral strike-slip fault (Sakınç et al., 1999), and is further crosscut by a series of E-W–trending faults. In drill core, these manifest as breccia zones up to 3 m thick, and at the surface they are recognized as small-scale faults with a typical ENE-WSW orientation, dipping approximately 60° to the east with throws of 0.7 to 1.5 m. A large-scale, N-S–trending normal fault bisects the deposit, down-throwing it to the west (Fig. 2).

The earliest intrusive phase at Muratdere is a granodiorite that is exposed as several discrete bodies at the surface, with diameters ranging from 200 m to 2.3 km, and with a minimum vertical extent of 300 m. The granodiorite is crosscut by a quartz-feldspar porphyry unit, which consists of phenocrysts of quartz, plagioclase feldspar, and minor biotite embedded in a quartzofeldspathic groundmass. The quartz-feldspar porphyry intrudes the granodiorite as branching vertical pipe-like bodies, with diameters ranging from 50 to 400 m and a minimum depth of 300 m (Figs. 2, 3). Both intrusive phases are mineralized and therefore predate the mineralization. The drill holes chosen for analysis in this paper are situated within the granodiorite and quartz-feldspar porphyry pipes to the east of the normal fault (Figs. 2, 3). Detailed drill core logging, coupled with XRD and SEM analysis, was used to determine the alteration and mineralization characteristics of the deposit.

*Alteration*

Within the core of the Muratdere deposit, which is exposed on the eastern side of the normal fault, both intrusive phases have been subjected to extensive potassic alteration (Fig. 4B, C), as well as silicification (Fig. 4F). Summary drill core logs of the distribution of alteration minerals (based on XRD analyses) with respect to intrusive phase and sulfide mineralogy are given in Figure 3. Potassic alteration is characterized by secondary potassium feldspar replacement of both phenocrystic and groundmass feldspars, generally causing complete replacement of the core (brown shading in alteration log in Fig. 3). Magnetite is also present within the potassic alteration, both disseminated in the groundmass and along thin veinlets (Fig. 4B). Secondary hydrothermal biotite replacement occurs in the granodiorite phase, with fine-grained biotite overgrowing primary biotite. Propylitic alteration occurs toward the base of the drill holes (between 95 and 290 m) characterized by chlorite, epidote, dolomite, and pyrite (Figs. 3, 4D, H). Drill core intervals that contain propylitic alteration have lower Au assay results than those with potassic alteration. Chlorite overprints some of the potassically altered zones in the center of the deposit (Fig. 3), replacing biotite phenocrysts.

The potassic core of the deposit is surrounded and partially overprinted by areas of intense chlorite-sericite alteration, characterized by the presence of smectite, illite, and sericite, and commonly associated with anhydrite and hematite. These alteration minerals replace feldspar phenocrysts. Secondary quartz alteration is also present as areas of silicification up to 12 m thick, where sections of the core may be replaced by quartz, commonly associated with anhydrite or barite (Fig. 4F, G). An advanced argillic overprint is observed around fractures and faults (Fig. 4G), with kaolinite, diaspore, pyrophyllite, and böhmite detected in the groundmass of fault breccias by XRD. The altered peridotite at the base of drill hole MDD 03 contains dolomite, talc, lizardite, and sepiolite.

*Mineralization*

The earliest mineralization within the quartz-feldspar porphyry is disseminated, microfracture-hosted pyrite, chalcopyrite, and molybdenite, which occurs within the zones of potassic alteration (Figs. 4B, F, 5). These sulfides are anhedral with rounded morphologies. The pyrite and chalcopyrite are intergrown, with rare microscopic galena grains located on boundaries, whereas the molybdenite crystals are spherical, and are commonly associated with chalcopyrite. Interstitial pyrite-chalcopyrite assemblages are also present, commonly with small inclusions of the host-rock minerals, including rutile and zircon. The remainder of the mineralization at Muratdere is associated with a series of crosscutting vein sets. The relative timings of these vein sets have been established by the crosscutting relationships (Fig. 6).

The first vein set (V1) comprises microcrystalline silica with an interlocking texture. The veins are 2 to 10 mm wide, with an average width of 8 mm, and are only found in regions of potassic alteration (Fig. 6). These are crosscut by a pyrite- and chalcopyrite-bearing set of veins (V2) that have straight to wavy margins, 5 to 30 mm wide, with the sulfides hosted in a central suture, and may be considered as "A veins" (Sillitoe, 2010). They commonly have a secondary potassium feldspar selvage and are found in areas of the core showing potassic alteration (Figs. 4C, 6).

The third vein set (V3) is also sulfide bearing, crosscuts V2, and is distinct in that it contains molybdenite as well as pyrite and chalcopyrite. These veins are 5 to 30 mm wide and irregular, and they contain equigranular quartz. The V3 veins have not developed vein selvages and occur in potassically altered areas of the core and zones with a mild propylitic and chlorite-sericite overprint. The sulfides are typically situated toward the center of the vein, although in some instances the molybdenite is concentrated along the vein margins (Figs. 4D, 6). Pyrite and chalcopyrite, when present, commonly enclose and postdate molybdenite. The molybdenite within the V3 veins displays a very distinctive bladed morphology in contrast to the spherical microfracture-hosted molybdenite (Fig. 5).

Vein set V4 consists of equigranular quartz veins that crosscut all previous vein sets. The V4 veins have sinuous margins and are 5 to 15 mm wide, with an average of 10 mm (Fig. 4A). They are found across the deposit and have a clay (illite-smectite) selvage, suggesting they are associated with chlorite-sericite alteration (Sillitoe, 2010).

Vein set V5 is polymetallic and is observed to cut V1, V3, and V4. These veins are irregular, typically 4 to 12 cm wide, with an average width of 5 cm. The veins comprise large, interlocking quartz and barite crystals with intergrown

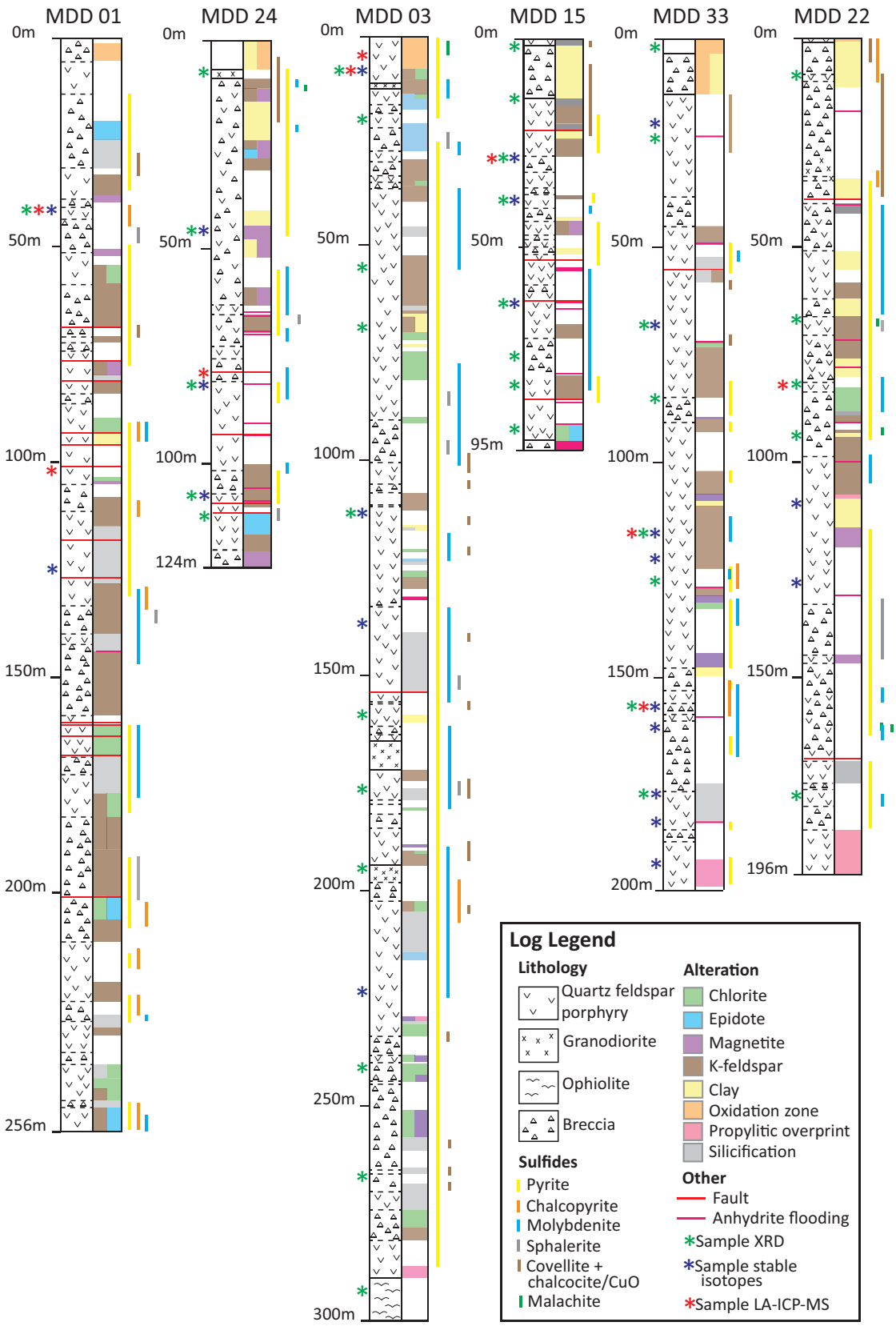


Fig. 3. Summary of drill core logging, showing the main geologic units and their relationships, the alteration zones within the deposit, and the presence of different types of sulfide. Sample points (made into thin sections) are marked by an asterisk, with the color representing the geochemical analysis performed on that sample. LA-ICP-MS = laser ablation-inductively coupled plasma-mass spectrometry, XRD = X-ray diffraction.

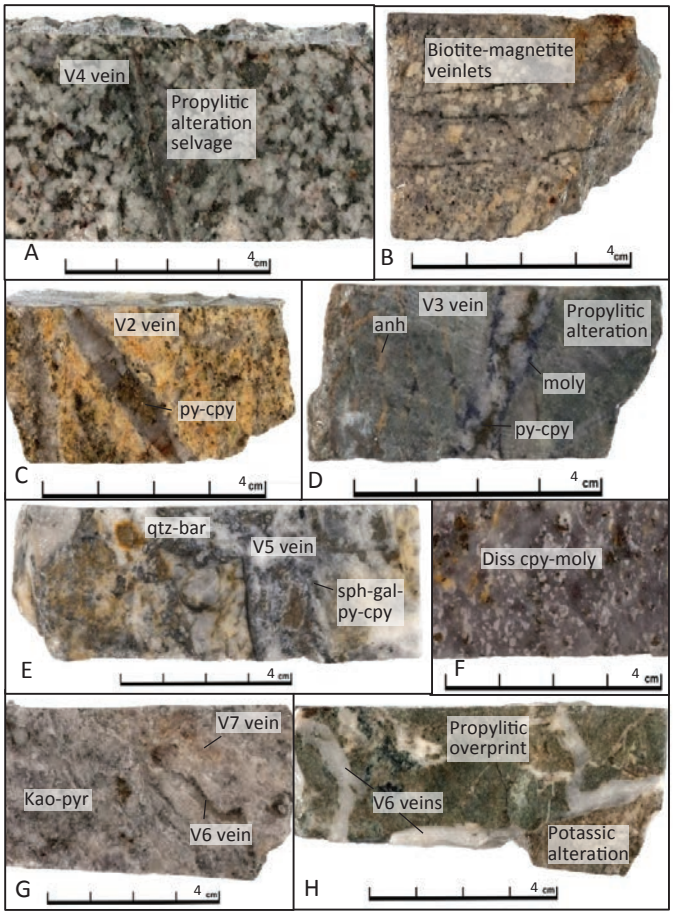


Fig. 4. Sections of drill core showing the main lithologies, vein sets, and alteration phases (anh = anhydrite, bar = barite, cpy = chalcopyrite, Diss = disseminated, gal = galena, kao = kaolinite, moly = molybdenite, py = pyrite, pyr = pyrophillite, qtz = quartz, sph = sphalerite). A) Granodiorite unit with V4 vein. B) Quartz-feldspar porphyry unit containing microfracture-hosted, disseminated molybdenite and chalcopyrite. C) V2 vein associated with intense potassic alteration, and minor propylitic overprint seen here as epidote alteration of feldspar. D) V3 vein with propylitic alteration and orange anhydrite veinlets. E) V5 vein. F) Silicified quartz-feldspar porphyry. G) V6 and V7 anhydrite veining associated with advanced argillic alteration. H) V6 anhydrite veining in altered quartz-feldspar porphyry.

sphalerite-galena-pyrite-chalcopyrite and rare molybdenite and pyrargite distributed throughout the vein. The V5 veins have a clay selvage including kaolinite, which is indicative of advanced argillic alteration (Sillitoe, 2010; Figs. 4E, 6). V5 veins are also associated with propylitic and chlorite-sericite alteration as well as extensive silicification. Vein set V6 comprises gray anhydrite with pyrite, which crosscut V1 to V5, as well as locally developed fault breccias. These veins are sinuous, ranging from 1 to 26 cm wide with an average of 8 cm, and have a kaolinite-pyrophyllite selvage (Fig. 4G). The veins comprise subhedral anhydrite crystals perpendicular to the vein margins and are consistent with syntaxial vein growth, with pyrite in a central suture. They are commonly observed in areas of intense advanced argillic alteration comprising smectite, illite, kaolinite, and pyrophyllite, as well as being associated with propylitic alteration (Fig. 4H).

The final vein set (V7) consists of pink anhydrite veins, which crosscut vein sets V1, V3, V5, and V6 and fault breccia.

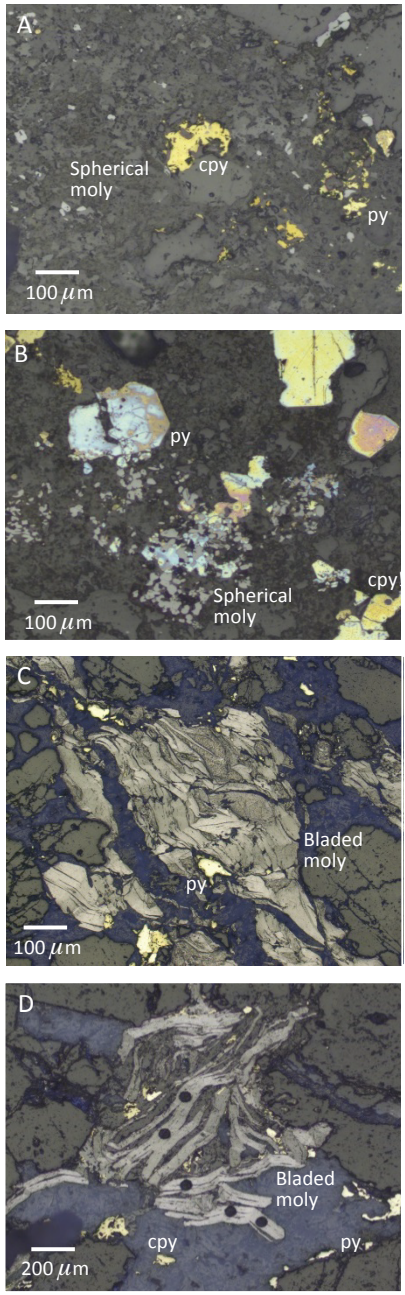


Fig. 5. Photomicrographs showing the two molybdenite generations under reflective light. A) and B) show spherical, microfracture-hosted molybdenite crystals (moly), chalcopyrite crystals (cpy), and pyrite crystals (py) disseminated within clay-altered potassium feldspar and quartz. C) and D) show bladed molybdenite crystals hosted in V3 quartz veins and intergrown with pyrite and chalcopyrite. D) also shows laser ablation-inductively coupled plasma-mass spectrometry (LA-ICP-MS) craters from trace element analysis.

This vein set is irregular, commonly branching, and ranges from 5 to 45 cm in width. These veins consist of anhedral anhydrite crystals and have a kaolinite-pyrophyllite selvage with rare dolomite alteration (Fig. 4G).

Industry whole-rock fire assay data for the Muratdere deposit shows maximum Re concentrations of up to 2.37 ppm, Au values of up to 1.35 ppm, Mo concentrations of up to 1,120 ppm, and Cu contents of up to 11,700 ppm in the mineralized host

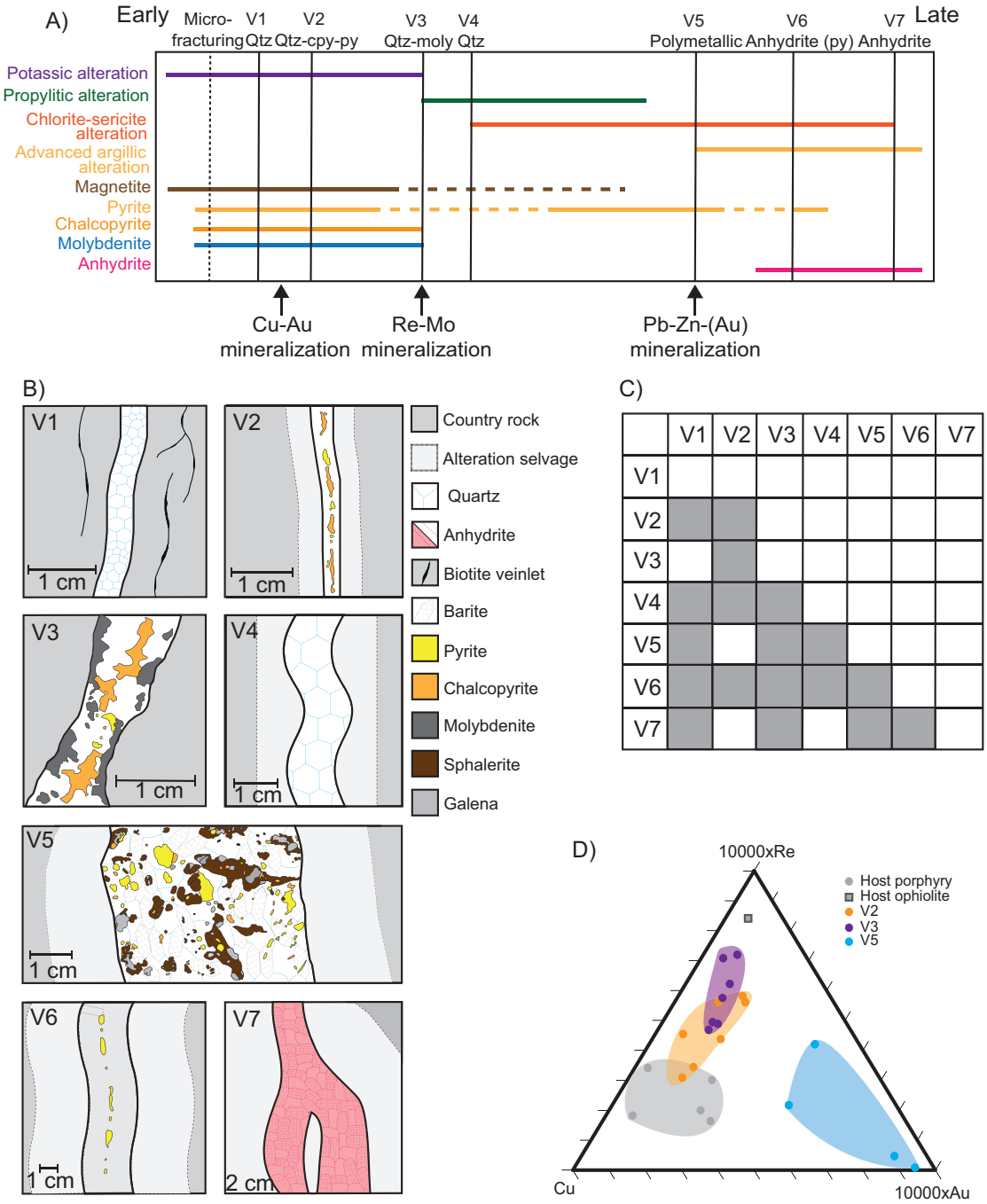


Fig. 6. Paragenetic diagram showing the following: A) The relative order of mineralizing and alteration events in the Muratdere deposit, with the main mineralization events highlighted (cpy = chalcopyrite, moly = molybdenite, py = pyrite, qtz = quartz). B) A schematic drawing showing the main features of each vein set. The quartz, sulfides, and sulfates depicted here were all analyzed for stable isotopes. C) Paragenetic diagram showing the crosscutting relationships of vein sets. D) Cu-Au-Re triplot showing the assay data for the three main mineralizing vein sets—V2, V3, and V5—illustrating their different metal endowment. The gray field represents assay data from unmineralized porphyry intrusions, and the gray square represents assay data from the ophiolitic country rock. V2 most closely matches the metal budget of the intrusion, while V3 is a mixture between that and the surrounding ophiolite. V5 has a very different metal budget from the other vein sets.

rocks; the deposit has a mean whole-rock assay Cu/Mo of 0.05 and Re/Mo of 0.003 (Stratex International, 2011, 2017). Whole-rock assay data from sections of drill core containing only one type of vein (where available) were compared with sections with no visible mineralization in order to estimate the effect of the different vein sets on metal content. When plotted on a Cu-Au-Re triplot (Fig. 6D), the assay data from V2 plots between the quartz-feldspar porphyry data and that for V3, whereas V3 plots toward the values from the altered peridotite country rock. V5 plots in a different area of the triplot,

showing a very different proportion of metals, characterized by elevated Au.

## Methods

A total of 1,160 m of core from six diamond drill holes into the Muratdere Cu-Mo (Au-Re) porphyry deposit was logged at a 5- to 10-m scale. Drill cores chosen for study are located within the core of the deposit, and the main features, rock types, alteration styles, and vein sets were recorded. Sections of interest were sampled for petrographic and geochemical study, ensuring all major lithologies, alteration types, and vein sets were represented. Thirty-two samples were made into polished thin sections and analyzed using both reflective and transmitted light microscopy.

### *SEM*

For SEM analyses, polished thin sections were analyzed on a LEO1450VP (variable pressure) electron microscope, located at the University of Southampton, equipped with a Princeton Tech, light element, energy-dispersive X-ray spectrometer and four quadrant backscattered electron detector, Type 222. Backscattered electron (BSE) images were used to constrain paragenetic relationships, while nonstandardized energy-dispersive spectroscopy (EDS) was used for first-pass mineral identification and semiquantitative analysis using spectrum indexes from the AzTec software package. The beam current used was 700 pA, with an accelerating voltage of 20 kV and a working distance of 19 mm. Further SEM analysis was undertaken at Cardiff University using a Zeiss Sigma HD field emission gun analytical SEM in order to identify any nanophases present within molybdenite crystals. The beam current used was 1.2 nA, with an accelerating voltage of 20 kV and a working distance of 8.9 mm.

### *EPMA*

EPMA-wavelength-dispersive spectroscopy (WDS) was used to map the distribution of Re across molybdenite crystals using the Natural History Museum (NHM) Cameca SX100 WDX electron microprobe. A beam current of 20 nA, an accelerating voltage of 20 keV, and a spot size of 1 $\mu$m were used to determine the following elements: S (K$\alpha$), Re (L$\alpha$), Pt (L$\alpha$), Mn (K$\alpha$), Fe (K$\alpha$), Co (K$\alpha$), Ni (K$\alpha$), Cu (K$\alpha$), Zn (K$\alpha$), As (L$\alpha$), Se (L$\alpha$), Pd (L$\alpha$), Ag (L$\alpha$), Sb (L$\alpha$), Te (L$\alpha$), Pb (M$\alpha$), Bi (M$\beta$), Cr (K$\alpha$), Ru (L$\alpha$), Rh (L$\alpha$), Os (M$\alpha$), Ir (L$\alpha$), Au (L$\alpha$), and Si (K$\alpha$). Major peak overlaps were performed prior to matrix correction, and a small number of minor empirical corrections obtained from standard data were applied to compensate for small peak overlaps. Quality assurance was performed on the NHM's in-house standard, with accuracy and precision defined as excellent for all elements (Piercey, 2014). However, Zn (K$\alpha$) and Re (L$\alpha$) have a large peak overlap (Rathkopf et al., 2017). Although sphalerite and other Zn-bearing minerals are not major phases in the samples analyzed and do not border molybdenite crystals, this means that the Re data presented in the maps should be treated as qualitative, and very bright areas are likely to represent sphalerite microinclusions (Fig. 7A).

### *XRD*

XRD analysis on 38 bulk-rock samples determined the alteration mineralogy, and detailed XRD clay mineral analysis was performed on eight samples. XRD analysis was performed at the University of Southampton, using a Philips X'Pert pro XRD instrument with a Cu X-ray tube, producing Cu K$\alpha$ X-rays. Each sample was crushed to <500 $\mu$m, and 1.5 g of sample and 0.5 g of corundum were added with isopropanol for further reduction on a micronizing mill. The samples were dried at 66°C, powdered using a pestle and mortar, and poured into a mount to prevent orientation of the crystal phases. A scan speed of 1.2°/min was used with data recorded every 0.02°$\Theta$. Mineral identification was undertaken using the JC powder diffraction studies database (www.icdd.com/index.php/pdf-4/). XRD analysis was also performed on two bulk molybdenite samples, prepared by scraping the molybdenite with a dental pick to create a powder before continuing the preparation and analysis as above.

### *LA-ICP-MS of sulfides*

As the Muratdere deposit contains two generations of molybdenite (Fig. 5), often within the same sample, these were analyzed using LA-ICP-MS. Eight polished thin section and polished block samples, hosting both molybdenite generations, were chosen for analysis. A total of 71 spot analyses were performed, 43 on bladed molybdenite and 28 on spherical molybdenite. Several spot analyses were performed on some large bladed molybdenite crystals. LA-ICP-MS analysis was also performed on pyrite crystals from V2 (n = 14), V3 (n = 23), and V5 (n = 10).

Polished thin sections were analyzed using a UP-213 New Wave laser ablation system with a wavelength of 213 nm. Ablated material was collected in an argon gas flow and fed into the plasma feed of a Thermo Scientific X-Series 2 ICP-mass spectrometer, housed at Cardiff University. The laser was operated at 15-Hz pulse rate with a dwell time of 40 s, and a gas blank measured for 30 s prior to acquisition. The ablation diameter was 55 $\mu$m. Trace element abundance was measured using the following isotopes: $^{57}$Fe, $^{59}$Co, $^{61}$Ni, $^{65}$Cu, $^{66}$Zn, $^{75}$As, $^{77}$Se, $^{95}$Mo, $^{99}$Ru, $^{103}$Rh, $^{105}$Pd, $^{108}$Pd, $^{109}$Ag, $^{111}$Cd, $^{121}$Sb, $^{125}$Te, $^{185}$Re, $^{189}$Os, $^{193}$Ir, $^{195}$Pt, $^{197}$Au, $^{206}$Pb, and $^{209}$Bi. Dwell times of 2 ms were used for major elements, 10 ms for semimetals, and 20 ms for PGEs. Limits of detection for all elements analyzed are given in Table 1.

Major element concentrations were measured prior to LA-ICP-MS analysis on the SEM, and $^{33}$S was used as an internal standard for trace element calibration. Measured isotopes were selected to avoid isobaric and polyatomic interferences, and $^{99}$Ru, $^{101}$Ru, $^{103}$Rh, $^{105}$Pd, $^{106}$Pd, and $^{108}$Pd were interference corrected. Machine calibration was performed using a series of five synthetic Ni-Fe-S quenched sulfide standards. The standards include Fe, Ni, Cu, and S as major elements and Co, Zn, As, Se, Ru, Rh, Pd, Ag, Cd, Sb, Te, Re, Os, Ir, Pt, Au, and Bi as trace elements, with compositions and analytical details for these standards available in Prichard et al. (2013). The standards produce five-point calibration curves for S, Ni, and Fe and three-point calibration curves for PGEs, Ag, Cd, Re, Au, Cu, Co, Zn, and semimetals. Gas blank subtraction and internal standard corrections were carried out on Thermo Plasmalab software. Accuracy and precision for Au and PGEs were checked by analyzing the Canada Centre for Mineral and Energy Technology (CANMET) Po727 Memorial standard as an unknown against the Cardiff quenched sulfide standards at the beginning and end

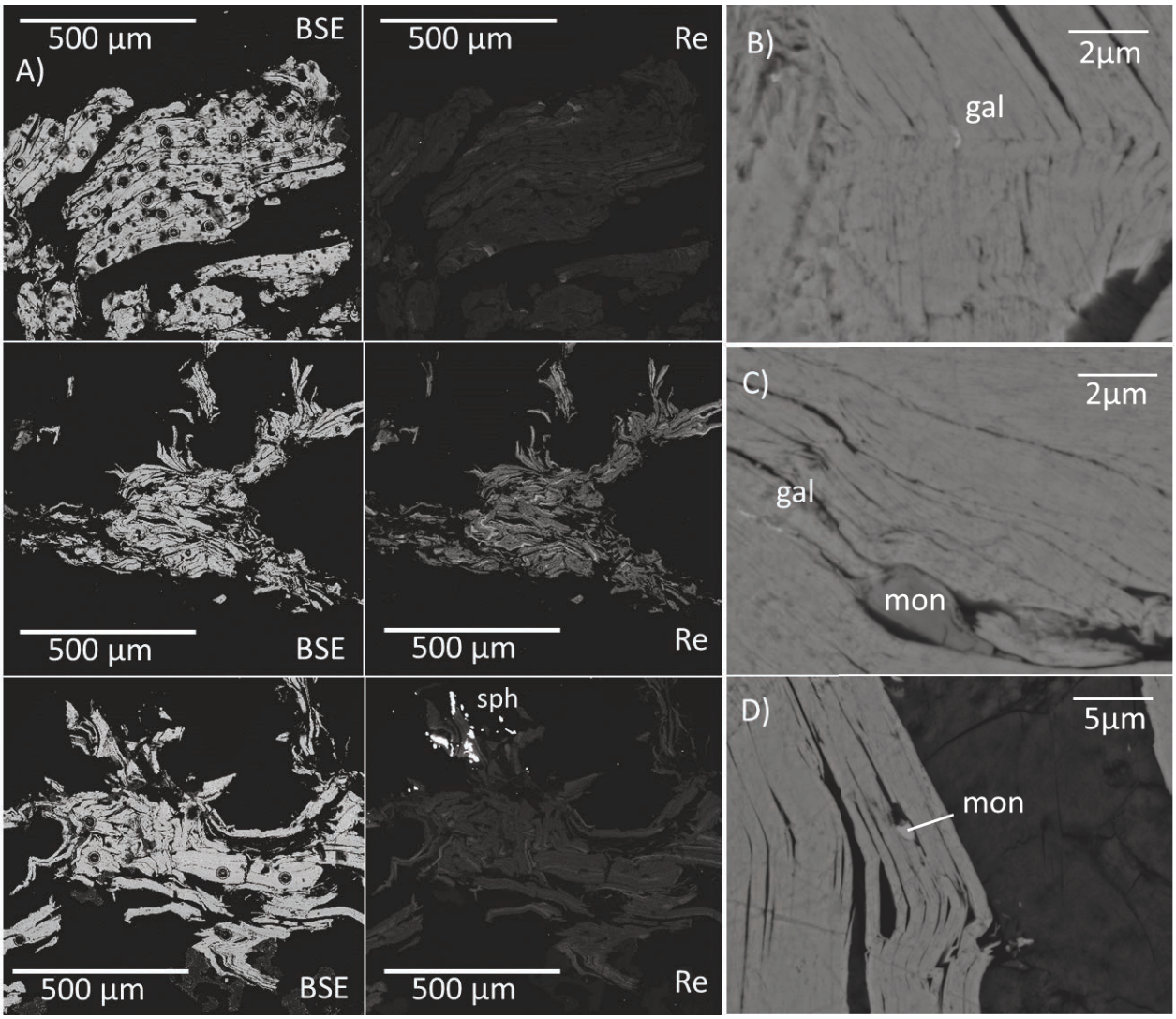


Fig. 7. A) Electron probe microanalysis (EPMA) maps of bladed molybdenite crystals from V3 veins in the Muratdere deposit showing heterogeneous Re zoning. The craters formed by laser ablation-inductively coupled plasma-mass spectrometry (LA-ICP-MS) analysis are visible in backscattered electron (BSE) imaging. The bright minerals in the bottom molybdenite are sphalerite (sph), which interferes with Re spectra. B) to D) BSE images from a high-resolution scanning electron microscope (SEM) survey of molybdenite crystals showing microinclusions of galena (gal) and monazite (mon). No telluride microinclusions were observed.

of each sample run (accuracy and precision given in App. 1, average $2\sigma$ = 2 ppm). The well-documented heterogeneity of Re concentrations in single molybdenite crystals (e.g., Ciobanu et al., 2013) makes repeat analyses difficult; however, $1\sigma$ precision based on time-resolved analysis (TRA) counting statistics is typically 10 to 30%. Representative TRA plots are given in Appendix 2. SEM survey was carried out prior to LA-ICP-MS analysis to identify any microinclusions present, and only sulfides without microinclusions visible on the SEM were analyzed. Care was also taken where possible to only quantify TRA intervals that did not show peaks in trace elements, which may indicate micro- or nanoinclusions.

*Stable isotopes*

*Sulfides and sulfates:* Sulfur isotope analyses of sulfides used two different methods—conventional analysis of handpicked sulfides and sulfates (after Robinson and Kusakabe, 1975, and Coleman and Moore, 1978, respectively) and laser analysis via in situ laser combustion (after Fallick et al., 1992) on sub-mm sulfides, or samples showing complex textural relationships prohibiting conventional picking. Initial $\delta^{66}SO_2$ data were converted to $\delta^{34}S$ values by calibration with international standards NBS-123 (17.1‰) and IAEA-S-3 (–31.5‰) for sulfides and NBS-127 for sulfates (21.2‰), as well as internal lab standard CP-1 (–4.6‰). Error of reproducibility, based on repeat analyses of standards, was about ±0.3‰ ($1\sigma$) for conventional analyses, and was estimated at about ±0.3‰ ($1\sigma$) for in situ laser analyses (Wagner et al., 2002). All sulfur isotope compositions were calculated relative to Vienna-Canyon Diablo Troilite (V-CDT) and are reported in standard notation.

*Oxygen and hydrogen:* Ten handpicked quartz separates were analyzed for O isotopes using a laser fluorination procedure,

Table 1. Results of In Situ LA-ICP-MS Analyses of Sulfides

| Sample no. | Vein set | Sulfide | Texture | S/Se | Co | As | Se | Ag | Sb | Te | Re | Au | Bi | Zn |
|---|---|---|---|---|---|---|---|---|---|---|---|---|---|---|
| LOD | | | | | 0.5 | 0.8 | 11 | 0.11 | 0.09 | 0.6 | 0.03 | 0.01 | 0.05 | 14 |
| MDD 33 155 | V3 | Molybdenite | Bladed | 1,713 | 2.5 | 3.1 | 234 | 3.44 | 0.15 | 4.4 | 445.21 | 2.53 | 4.17 | <14 |
| MDD 33 155 | V3 | Molybdenite | Bladed | 2,103 | 0.4 | <0.8 | 191 | 0.22 | 0.18 | 0.7 | 516.37 | 0.10 | 0.16 | 15 |
| MDD 33 155 | V3 | Molybdenite | Bladed | 2,262 | 0.3 | <0.8 | 177 | 0.24 | <0.09 | 1.1 | 316.29 | 0.10 | 0.28 | <14 |
| MDD 33 155 | V3 | Molybdenite | Bladed | 2,141 | 0.3 | <0.8 | 187 | 0.19 | <0.09 | 1.0 | 328.73 | 0.07 | 0.47 | <14 |
| MDD 33 155 | V3 | Molybdenite | Bladed | 2,548 | 0.5 | 1.9 | 157 | 0.32 | 0.11 | <0.6 | 415.69 | 0.04 | 0.38 | <14 |
| MDD 33 155 | V3 | Molybdenite | Bladed | 1,681 | 1.2 | 4.3 | 238 | 0.54 | 0.18 | 1.3 | 4,000.53 | 0.05 | 0.09 | <14 |
| MDD 33 155 | V3 | Molybdenite | Bladed | 1,684 | 1.9 | 3.3 | 238 | 0.65 | 0.22 | 2.4 | 3,310.43 | 0.22 | 2.20 | <14 |
| MDD 33 155 | V3 | Molybdenite | Bladed | 1,744 | 1.6 | 4.9 | 230 | 0.79 | 0.18 | 0.8 | 510.08 | 0.09 | 0.25 | <14 |
| MDD 33 155 | V3 | Molybdenite | Bladed | 2,310 | 3.1 | 5.8 | 174 | 1.86 | 0.11 | 3.4 | 568.35 | 0.90 | 2.68 | <14 |
| MDD 33 155 | V3 | Molybdenite | Bladed | 2,283 | 7.1 | 13.6 | 176 | 2.10 | 0.55 | 3.4 | 751.59 | 0.59 | 2.64 | <14 |
| MDD 33 155 | V3 | Molybdenite | Bladed | 2,452 | 1.4 | 2.8 | 164 | 2.53 | 0.54 | 4.1 | 546.69 | 0.62 | 6.27 | <14 |
| MDD 33 155 | V3 | Molybdenite | Bladed | 2,310 | 0.7 | 3.7 | 174 | 0.73 | 0.18 | 1.4 | 837.30 | 0.16 | 0.46 | <14 |
| MDD 33 155 | V3 | Molybdenite | Bladed | 1,998 | 0.7 | 1.4 | 201 | 0.25 | 0.13 | 1.6 | 615.77 | 0.11 | 0.39 | <14 |
| MDD 33 155 | V3 | Molybdenite | Bladed | 2,265 | 0.9 | <0.8 | 177 | 0.52 | <0.09 | <0.6 | 1,006.97 | 0.11 | 0.37 | <14 |
| MDD 33 155 | V3 | Molybdenite | Bladed | 2,358 | 0.7 | <0.8 | 170 | 0.90 | <0.09 | 1.5 | 660.26 | 0.23 | 0.85 | <14 |
| MDD 33 155 | V3 | Molybdenite | Bladed | 2,471 | 1.6 | 3.8 | 162 | 0.80 | 0.14 | 2.7 | 755.36 | 0.25 | 1.83 | <14 |
| MDD 33 155 | V3 | Molybdenite | Bladed | 1,947 | 3.6 | 6.7 | 206 | 2.33 | 0.28 | 2.0 | 310.95 | 0.39 | 1.16 | 16 |
| MDD 33 155 | V3 | Molybdenite | Bladed | 1,934 | 0.8 | <0.8 | 207 | 0.60 | <0.09 | 0.7 | 1,364.47 | 0.08 | 0.62 | 25 |
| MDD 33 155 | V3 | Molybdenite | Bladed | 2,014 | 2.2 | 2.3 | 199 | 1.31 | 0.14 | 2.4 | 1,344.84 | 0.30 | 1.14 | 44 |
| MDD 33 155 | V3 | Molybdenite | Bladed | 1,852 | 1.7 | <0.8 | 216 | 0.34 | <0.09 | 0.6 | 1,249.64 | <0.01 | 0.19 | <14 |
| MDD 33 155 | V3 | Molybdenite | Bladed | 2,074 | 4.1 | 9.8 | 193 | 3.09 | 0.40 | 1.3 | 906.47 | 0.18 | 1.06 | <14 |
| MDD 33 155 | V3 | Molybdenite | Bladed | 1,924 | 0.2 | <0.8 | 208 | 0.12 | <0.09 | <0.6 | 1,347.17 | <0.01 | 0.01 | <14 |
| MDD 33 155 | V3 | Molybdenite | Bladed | 2,221 | 0.7 | 2.1 | 181 | 0.41 | 0.17 | <0.6 | 228.07 | 0.06 | 1.01 | <14 |
| MDD 33 155 | V3 | Molybdenite | Bladed | 1,936 | 1.8 | 3.8 | 207 | 1.26 | 0.19 | 1.8 | 1,159.38 | 0.23 | 0.70 | 15 |
| MDD 33 155 | V3 | Molybdenite | Bladed | 1,956 | 17.1 | 27.5 | 205 | 30.97 | 0.83 | 6.6 | 936.42 | 20.09 | 8.84 | 21 |
| MDD 33 155 | V3 | Molybdenite | Bladed | 2,237 | 6.7 | 13.9 | 179 | 9.60 | 0.63 | 4.9 | 1,613.05 | 0.97 | 2.65 | 22 |
| MDD 33 155 | V3 | Molybdenite | Bladed | 1,827 | 6.4 | 5.3 | 219 | 3.45 | 0.23 | 1.6 | 1,672.62 | 0.62 | 2.40 | 15 |
| MDD 03 12 | V3 | Molybdenite | Bladed | 2,387 | 0.3 | <0.8 | 168 | 0.54 | <0.09 | <0.6 | 828.93 | 0.06 | 0.25 | <14 |
| MDD 03 12 | V3 | Molybdenite | Bladed | 2,093 | 1.2 | <0.8 | 192 | 2.04 | 0.11 | 1.3 | 1,385.22 | 0.15 | 1.63 | 15 |
| MDD 03 12 | V3 | Molybdenite | Bladed | 2,636 | 1.9 | 1.4 | 152 | 7.88 | 0.41 | 1.4 | 746.76 | 1.27 | 1.95 | 182 |
| MDD 03 12 | V3 | Molybdenite | Bladed | 2,342 | 1.3 | <0.8 | 171 | 4.75 | 0.36 | 1.0 | 913.03 | 0.18 | 1.45 | 63 |
| MDD 33 155 | V3 | Molybdenite | Bladed | | 1.8 | 9.5 | <11 | 2.90 | 0.91 | 1.55 | 2,038.53 | 0.34 | 1.11 | 22 |
| MDD 33 155 | V3 | Molybdenite | Bladed | 2,301 | 3.7 | 12.7 | 174 | 4.71 | 0.52 | 1.75 | 537.97 | 0.20 | 0.80 | 19 |
| MDD 33 155 | V3 | Molybdenite | Bladed | 2,432 | 1.4 | 2.6 | 165 | 1.03 | 0.14 | 1.79 | 2,142.20 | 0.06 | 0.41 | <16 |
| MDD 33 155 | V3 | Molybdenite | Bladed | 2,198 | 4.8 | 1.8 | 182 | 2.15 | <0.12 | 1.82 | 711.78 | 0.10 | 0.97 | <16 |
| MDD 33 155 | V3 | Molybdenite | Bladed | 3,524 | 0.5 | <0.9 | 114 | 0.21 | <0.12 | 0.70 | 1,427.14 | 0.03 | 0.09 | 1,201 |
| MDD 22 84 | V3 | Molybdenite | Bladed | 3,612 | 2.8 | 5.1 | 111 | 1.52 | 0.82 | <0.65 | 1,595.75 | 0.09 | 0.27 | 1,650 |
| MDD 22 84 | V3 | Molybdenite | Bladed | 3,765 | 0.6 | <0.9 | 107 | 2.11 | <0.12 | 1.47 | 1,322.28 | <0.01 | 0.51 | 11,539 |
| MDD 22 84 | V3 | Molybdenite | Bladed | 4,490 | 2.5 | 1.5 | 89 | 1.76 | 0.60 | 1.39 | 1,765.26 | 0.13 | 0.81 | 107 |
| MDD 22 84 | V3 | Molybdenite | Bladed | 3,592 | 1.1 | 2.7 | 112 | 1.15 | 0.61 | 1.08 | 1,170.02 | 0.16 | 1.09 | 705 |
| MDD 22 84 | V3 | Molybdenite | Bladed | 4,070 | 9.4 | 18.1 | 99 | 6.78 | 2.45 | 6.71 | 1,478.22 | 0.28 | 5.57 | 375 |
| MDD 22 84 | V3 | Molybdenite | Bladed | 4,225 | 2.3 | 5.0 | 95 | 6.74 | 0.61 | 5.11 | 1,404.11 | 0.46 | 2.76 | 280 |
| MDD 22 84 | V3 | Molybdenite | Bladed | 3,970 | 2.1 | 5.5 | 101 | 5.34 | 1.01 | 6.40 | 1,159.88 | 0.39 | 3.68 | 278 |
| MDD 33 155 | V3 | Molybdenite | Spherical | 1,936 | 0.4 | <0.8 | 207 | <0.11 | <0.09 | 1.0 | 484.29 | <0.01 | 0.10 | <14 |
| MDD 33 155 | V3 | Molybdenite | Spherical | 2,309 | 0.5 | <0.8 | 174 | 0.43 | <0.09 | 0.7 | 284.96 | 0.05 | 0.46 | <14 |
| MDD 33 155 | V3 | Molybdenite | Spherical | 2,167 | 3.3 | 2.4 | 185 | 2.32 | <0.09 | 6.2 | 415.15 | 0.22 | 1.72 | 32 |
| MDD 33 155 | V3 | Molybdenite | Spherical | 1,775 | 0.1 | <0.8 | 226 | <0.11 | <0.09 | 0.7 | 497.72 | <0.01 | <0.04 | <14 |
| MDD 33 155 | V3 | Molybdenite | Spherical | 1,888 | 0.1 | <0.8 | 212 | <0.11 | <0.09 | <0.6 | 526.61 | <0.01 | <0.04 | <14 |
| MDD 33 118 | V3 | Molybdenite | Spherical | 1,776 | 0.7 | <0.9 | 226 | 2.89 | 0.30 | 1.42 | 200.59 | 0.11 | 7.81 | 21 |
| MDD 33 118 | V3 | Molybdenite | Spherical | 3,394 | <0.5 | <0.9 | 118 | <0.15 | 0.14 | 2.57 | 279.10 | <0.01 | 0.71 | <16 |
| MDD 33 118 | V3 | Molybdenite | Spherical | 2,019 | 0.5 | <0.9 | 199 | 1.04 | 0.25 | 2.17 | 464.82 | 0.05 | 7.26 | 42 |
| MDD 33 118 | V3 | Molybdenite | Spherical | 1,626 | 1.1 | <0.9 | 247 | 3.04 | <0.12 | 1.94 | 290.32 | 0.07 | 1.85 | 19 |
| MDD 33 118 | V3 | Molybdenite | Spherical | 1,507 | 1.7 | 2.4 | 266 | 23.22 | 2.56 | 2.35 | 577.84 | 4.66 | 5.14 | 32 |
| MDD 33 118 | V3 | Molybdenite | Spherical | 2,086 | 1.8 | 2.8 | 192 | 33.64 | 1.78 | 3.35 | 1,027.12 | 5.36 | 6.24 | 54 |
| MDD 33 118 | V3 | Molybdenite | Spherical | 1,715 | <0.5 | <0.9 | 234 | 0.25 | <0.12 | <0.65 | 556.60 | <0.01 | 1.76 | <16 |
| MDD 33 118 | V3 | Molybdenite | Spherical | 1,927 | <0.5 | <0.9 | 208 | 0.77 | <0.12 | 1.27 | 321.84 | 0.03 | 8.87 | <16 |
| MDD 33 118 | V3 | Molybdenite | Spherical | 1,738 | 7.5 | 2.3 | 231 | 10.62 | 1.51 | 4.44 | 625.01 | 0.49 | 17.62 | 35 |
| MDD 33 118 | V3 | Molybdenite | Spherical | 1,697 | <0.5 | <0.9 | 236 | 0.61 | <0.12 | 1.29 | 133.97 | 0.03 | 10.78 | 30 |
| MDD 33 118 | V3 | Molybdenite | Spherical | 1,578 | 0.6 | 1.0 | 254 | 0.64 | <0.12 | 1.55 | 250.68 | 0.02 | 0.66 | 40 |
| MDD 33 118 | V3 | Molybdenite | Spherical | 1,514 | <0.5 | <0.9 | 265 | 1.39 | <0.12 | 0.72 | 201.76 | <0.01 | 0.87 | <16 |
| MDD 33 118 | V3 | Molybdenite | Spherical | 1,904 | 0.5 | <0.9 | 211 | 0.85 | 0.16 | 2.81 | 613.27 | 0.06 | 9.42 | <16 |
| MDD 33 118 | V3 | Molybdenite | Spherical | 1,638 | 2.0 | 3.3 | 245 | 7.59 | 1.59 | 4.26 | 900.21 | 0.30 | 9.09 | 23 |
| MDD 33 155 | V3 | Molybdenite | Spherical | 2,508 | 1.6 | 2.1 | 160 | 1.26 | <0.12 | 2.16 | 770.68 | 0.08 | 2.65 | 103 |
| MDD 33 155 | V3 | Molybdenite | Spherical | 2,761 | 2.6 | 1.1 | 145 | <0.15 | <0.12 | 1.71 | 484.12 | 0.17 | 0.98 | <16 |
| MDD 33 155 | V3 | Molybdenite | Spherical | 2,597 | 5.1 | 10.1 | 154 | 0.83 | 0.18 | 2.09 | 411.97 | 0.16 | 0.41 | <16 |
| MDD 33 155 | V3 | Molybdenite | Spherical | 2,288 | 15.3 | 10.6 | 175 | 1.93 | 0.31 | 2.79 | 588.90 | 0.33 | 1.26 | <16 |
| MDD 33 155 | V3 | Molybdenite | Spherical | 2,049 | <0.5 | <0.9 | 196 | <0.15 | <0.12 | <0.65 | 216.87 | <0.01 | <0.05 | <16 |
| MDD 33 155 | V3 | Molybdenite | Spherical | 1,684 | <0.5 | <0.9 | 238 | 0.09 | <0.12 | <0.65 | 201.38 | <0.01 | <0.05 | <16 |

Table 1. *(Cont.)*

| Sample no. | Vein set | Sulfide | Texture | S/Se | Co | As | Se | Ag | Sb | Te | Re | Au | Bi | Zn |
|---|---|---|---|---|---|---|---|---|---|---|---|---|---|---|
| MDD 33 155 | V3 | Molybdenite | Spherical | 2,201 | 8.7 | 1.1 | 182 | 2.41 | 0.78 | 7.14 | 789.08 | 0.88 | 3.42 | 82 |
| MDD 33 155 | V3 | Molybdenite | Spherical | 3,930 | 2.2 | 1.7 | 102 | 2.09 | 0.44 | 0.94 | 1,858.91 | 0.12 | 0.65 | 491 |
| MDD 33 155 | V3 | Molybdenite | Spherical | 3,925 | 0.8 | <0.9 | 102 | 4.76 | <0.12 | 0.69 | 1,881.57 | 0.03 | 0.58 | 30 |
| MDD 33 155 | V2 | Pyrite | | 3,818 | 126.6 | 1.0 | 140 | 0.13 | <0.09 | 0.7 | <0.03 | 0.21 | 0.17 | <14 |
| MDD 03 12 | V2 | Pyrite | | 12,728 | 122.0 | 8.6 | 42 | 0.45 | <0.09 | <0.6 | 1.88 | 0.33 | 6.37 | 284 |
| MDD 03 12 | V2 | Pyrite | | 15,074 | 59.9 | 22.6 | 35 | 0.40 | <0.09 | <0.6 | 1.48 | 0.11 | 2.30 | 222 |
| MDD 03 12 | V2 | Pyrite | | 8,894 | 268.5 | 2.3 | 60 | <0.11 | <0.09 | 1.3 | 3.40 | <0.01 | 0.31 | <14 |
| MDD 03 12 | V2 | Pyrite | | 12,872 | 338.3 | 27.9 | 42 | <0.11 | <0.09 | 0.6 | 0.44 | <0.01 | <0.04 | <14 |
| MDD 03 12 | V2 | Pyrite | | 9,749 | 254.1 | <0.8 | 55 | <0.11 | <0.09 | <0.6 | 0.63 | <0.01 | <0.04 | 16 |
| MDD 03 12 | V2 | Pyrite | | 11,436 | 234.3 | <0.8 | 47 | <0.11 | <0.09 | <0.6 | 0.39 | <0.01 | <0.04 | <14 |
| MDD 33 42 | V2 | Pyrite | | 9,163 | 43.1 | <0.9 | 58 | <0.15 | <0.12 | 4.60 | <0.03 | <0.01 | 0.75 | 43 |
| MDD 33 42 | V2 | Pyrite | | 31,493 | 77.4 | 5.4 | 17 | 0.41 | 1.10 | 4.46 | <0.03 | 0.05 | 3.72 | 305 |
| MDD 33 42 | V2 | Pyrite | | 26,877 | 21.8 | 6.0 | 20 | 0.27 | 1.03 | 8.40 | <0.03 | <0.01 | 5.04 | 290 |
| MDD 33 42 | V2 | Pyrite | | 22,753 | 27.3 | 4.1 | 24 | 1.13 | 0.84 | 10.66 | <0.03 | 0.10 | 5.07 | 261 |
| MDD 33 42 | V2 | Pyrite | | 27,201 | 13.4 | 5.0 | 20 | 0.85 | 1.05 | 1.98 | <0.03 | 0.21 | 2.41 | 434 |
| MDD 33 42 | V2 | Pyrite | | 18,993 | 16.9 | 12.6 | 28 | 0.42 | 2.81 | 13.93 | <0.03 | 0.09 | 12.04 | 656 |
| MDD 33 42 | V2 | Pyrite | | 16,677 | 80.3 | 262.4 | 32 | 19.04 | 277.14 | 35.98 | <0.03 | 0.25 | 17.60 | 2,034 |
| MDD 33 118 | V3 | Pyrite | | 8,119 | 265.9 | 3.4 | 66 | 0.75 | 0.65 | <0.65 | 0.63 | 0.03 | 4.71 | 187 |
| MDD 33 118 | V3 | Pyrite | | 5,565 | 379.8 | 14.7 | 96 | 65.36 | 1.45 | 1.77 | 3.66 | 1.06 | 2.26 | 306 |
| MDD 33 118 | V3 | Pyrite | | 14,956 | 391.3 | 3.9 | 36 | 2.29 | 0.44 | 0.58 | 0.14 | 0.16 | 5.03 | 49 |
| MDD 33 118 | V3 | Pyrite | | 6,396 | 110.9 | 1.5 | 84 | 0.45 | <0.12 | 1.16 | <0.03 | 0.07 | 1.57 | 237 |
| MDD 33 155 | V3 | Pyrite | | 5,198 | 1,228.6 | 14.3 | 103 | <0.15 | <0.12 | <0.65 | 0.09 | <0.01 | 1.41 | <16 |
| MDD 33 155 | V3 | Pyrite | | 6,114 | 1.4 | <0.9 | 88 | 0.88 | <0.12 | <0.65 | 0.18 | 0.05 | 0.85 | <16 |
| MDD 33 155 | V3 | Pyrite | | 16,725 | 66.0 | 3.2 | 32 | 11.12 | 0.26 | 6.16 | <0.03 | 0.90 | 55.22 | 198 |
| MDD 33 155 | V3 | Pyrite | | 5,959 | 130.0 | 14.5 | 90 | 45.28 | 1.95 | 32.53 | 0.30 | 1.71 | 73.54 | 29 |
| MDD 33 155 | V3 | Pyrite | | 8,770 | 6.3 | 0.9 | 61 | 5.82 | 0.16 | 1.60 | <0.03 | 0.02 | 2.95 | <16 |
| MDD 33 155 | V3 | Pyrite | | 4,499 | 949.3 | 713.7 | 119 | 1.33 | <0.12 | 1.45 | 0.04 | 0.04 | 1.30 | 17 |
| MDD 33 155 | V3 | Pyrite | | 6,690 | 836.1 | 137.3 | 80 | 2.16 | 0.16 | 0.64 | 0.19 | 0.18 | 4.89 | 64 |
| MDD 33 155 | V3 | Pyrite | | 4,319 | 840.7 | 158.9 | 124 | 0.51 | <0.12 | 1.06 | 0.14 | 0.19 | 1.50 | 17 |
| MDD 33 155 | V3 | Pyrite | | 5,452 | <0.5 | 1.1 | 98 | 5.24 | <0.12 | 1.09 | <0.03 | 0.59 | 0.20 | 20 |
| MDD 33 155 | V3 | Pyrite | | 12,691 | 1.6 | <0.9 | 42 | 0.56 | <0.12 | <0.65 | 0.07 | 0.00 | <0.05 | 17 |
| MDD 33 155 | V3 | Pyrite | | 6,308 | 2.4 | 2.0 | 85 | 4.06 | 0.38 | 0.88 | <0.03 | 0.24 | 0.73 | 25 |
| MDD 33 155 | V3 | Pyrite | | 7,943 | 7,125.2 | <0.9 | 67 | <0.15 | <0.12 | <0.65 | <0.03 | <0.01 | <0.05 | <16 |
| MDD 33 155 | V3 | Pyrite | | 21,996 | 106.3 | 18.7 | 24 | 21.09 | 1.07 | 8.09 | <0.03 | 0.26 | 18.51 | 187 |
| MDD 33 155 | V3 | Pyrite | | 3,891 | 4,170.5 | 162.9 | 137 | <0.15 | <0.12 | 0.70 | 0.20 | <0.01 | 0.14 | <16 |
| MDD 33 155 | V3 | Pyrite | | 4,175 | 115.4 | 2,230.7 | 128 | 1.18 | 8.23 | <0.65 | <0.03 | 2.26 | 2.69 | 62 |
| MDD 33 155 | V3 | Pyrite | | 12,335 | 1.6 | <0.9 | 43 | 0.47 | <0.12 | <0.65 | <0.03 | <0.01 | 0.01 | 6,678 |
| MDD 22 84 | V3 | Pyrite | | 3,175 | 841.3 | 125.8 | 169 | 0.64 | 1.86 | 1.96 | 0.13 | 0.52 | 3.30 | 123 |
| MDD 22 84 | V3 | Pyrite | | 14,077 | 122.0 | 5.3 | 38 | 1.15 | 1.54 | 1.68 | 0.06 | 0.22 | 2.14 | 219 |
| MDD 22 84 | V3 | Pyrite | | 38,585 | 9.1 | <0.9 | 14 | <0.15 | <0.12 | <0.65 | <0.03 | <0.01 | <0.05 | 14 |
| MDD 15 39 | V5 | Pyrite | | 9,562 | 36.8 | <0.9 | 56 | <0.15 | <0.12 | <0.65 | <0.03 | <0.01 | <0.05 | <16 |
| MDD 15 39 | V5 | Pyrite | | 11,805 | 186.4 | 11.3 | 45 | 0.33 | 1.22 | <0.65 | <0.03 | 0.12 | 0.67 | 28 |
| MDD 15 39 | V5 | Pyrite | | 12,931 | 109.6 | 3.7 | 41 | 0.97 | 0.44 | 0.88 | 0.04 | 0.17 | 0.56 | 51 |
| MDD 15 39 | V5 | Pyrite | | 9,025 | 394.1 | 6.4 | 59 | 1.02 | 0.85 | 0.08 | <0.03 | 0.03 | <0.05 | 65 |
| MDD 15 39 | V5 | Pyrite | | 27,263 | 25.7 | 1.2 | 20 | 0.22 | 0.17 | <0.65 | <0.03 | 0.04 | 2.74 | 583 |
| MDD 15 39 | V5 | Pyrite | | 24,302 | 9.3 | <0.9 | 22 | <0.15 | <0.12 | 0.75 | <0.03 | <0.01 | 0.18 | <16 |
| MDD 15 39 | V5 | Pyrite | | 21,509 | 277.6 | 0.9 | 25 | 0.41 | 0.14 | <0.65 | 0.05 | <0.01 | 0.11 | 22 |
| MDD 15 39 | V5 | Pyrite | | 25,085 | 150.7 | 6.9 | 21 | 1.93 | 1.71 | 0.92 | 2.54 | 0.17 | 0.89 | 25 |
| MDD 15 39 | V5 | Pyrite | | 21,488 | 9.2 | 1.0 | 25 | 1.35 | <0.12 | <0.65 | <0.03 | 0.13 | 1.42 | 83 |
| MDD 15 39 | V5 | Pyrite | | 45,341 | 22.5 | 9.0 | 12 | 2.95 | 1.13 | <0.65 | <0.03 | 0.17 | 2.80 | 950 |

Note: Trace element concentrations of molybdenite and pyrite samples in ppm
Abbreviations: LA-ICP-MS = laser ablation-inductively coupled plasma-mass spectrometry, LOD = limit of detection

involving total sample reaction with excess $ClF_3$ using a $CO_2$ laser at temperatures in excess of 1,500°C (Sharp, 1990). All fluorination experiments resulted in 100% release of $O_2$ from the silicate lattice. This $O_2$ was converted to $CO_2$ by reaction with hot graphite and analyzed by a VG SIRA II spectrometer. Results are reported in standard notation ($\delta^{18}O$) as ‰ deviations from Vienna-Standard Mean Ocean Water (V-SMOW). Error of reproducibility was typically about ±0.3‰ during analyses.

Hydrogen analysis was done by in vacuo bulk heating. One-gram bulk samples of quartz were analyzed using the method of Donnelly et al. (2001) and a VG-Micromass Optima mass spectrometer. Samples were heated to a maximum of 700°C to release included fluids (but not molecular hydroxides; Gleeson et al., 2008). Results are reported in standard notation ($\delta$D) as ‰ deviations from V-SMOW. Error of reproducibility is typically about ±5‰ during analyses.

## Analytical Results

### *Trace elements in sulfides*

*Trace elements in molybdenite:* The molybdenite crystals analyzed contain highly variable Re concentrations (Table 1, full

results in App. 3). The mean for all molybdenite generations in Muratdere is 904 ppm ($\sigma$ = 687, n = 71), with a range between 134 and 4,001 ppm. This is above the range and average Re content of molybdenite in porphyry deposits globally (690 ppm, Fig. 8C). The large range of Re concentration within molybdenite crystals is similar to that reported for other porphyry deposits globally, and the Re concentrations in the molybdenite samples show no correlation with any other trace elements within the deposit (Fig. 9). The molybdenite samples from Muratdere also contain an average of 183 ppm Se ($\sigma$ = 44, n = 71), with an average S/Se of 2,361 ppm ($\sigma$ = 729, n = 71).

Unlike Re and Se, which were present in all molybdenite samples analyzed (n = 71), the other trace elements analyzed were only above detection limit in some of the crystals. The molybdenite samples that contain all trace elements have mean concentrations of 3.1 ppm Co ($\sigma$ = 3.4, n = 51), 5.4 ppm As ($\sigma$ = 5.2, n = 42), 3.2 ppm Ag ($\sigma$ = 6, n = 68), 0.4 ppm Sb ($\sigma$ = 0.5, n = 58), and 2.4 ppm Bi ($\sigma$ = 3.2, n = 71).

The only elements that show correlation in Muratdere molybdenite samples are As and Co, which have a Pearson correlation coefficient of 0.7, Au and Co (Pearson = 0.6), Au and As (Pearson = 0.6), Sb and Ag (Pearson = 0.6), Te and Co (Pearson = 0.6), and Au and Ag (Pearson = 0.8; Fig. 9). Time-resolved LA-ICP-MS data for Te, Bi, Sb, Ag, and Au show irregular profiles, with short intervals of elevated concentrations (App. 2). This may be due to the presence of nanophases or small mineral inclusions (e.g., electrum) within the molybdenite.

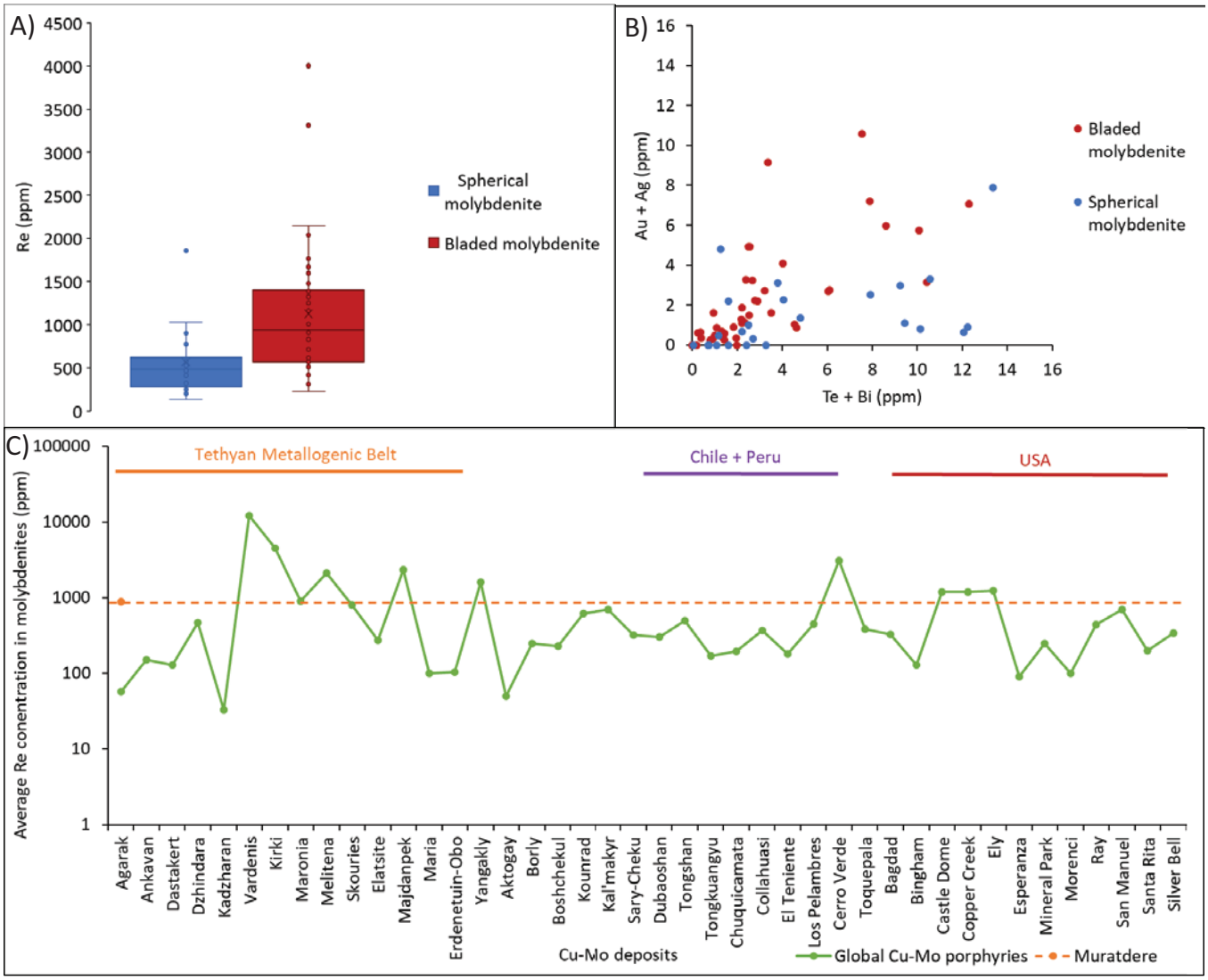


Fig. 8. A) Box plot showing the results of individual laser ablation-inductively coupled plasma-mass spectrometry (LA-ICP-MS) analyses for Re in the two molybdenite generations representing the mean, quartiles, and outliers. The early microfracture-hosted spherical molybdenite (blue) contains significantly less Re than the later vein-hosted bladed molybdenite (red). B) Plot showing Au + Ag concentrations of molybdenite samples against Te + Bi. The positive correlation suggests the presence of precious metal mineral microinclusions. C) Plot showing the average concentration of Re in molybdenite samples from Cu-Mo porphyry deposits globally (data from Berzina et al., 2005; Singer et al., 2005; Grabezhev, 2007; Voudouris et al., 2009; Grabezhev and Voudouris, 2014), compared to the average concentration of Re in molybdenite in Muratdere (dashed orange line). Different deposit locations are labeled.

| | Co | Cu | Zn | As | Se | Mo | Ag | Sb | Te | Re | Au | Bi |
|---|---|---|---|---|---|---|---|---|---|---|---|---|
| **Co** | 1.0 | <dl | -0.1 | **0.7** | 0.0 | -0.2 | 0.4 | 0.2 | **0.6** | 0.0 | **0.6** | 0.3 |
| **Cu** | -0.1 | 1.0 | <dl | <dl | <dl | <dl | <dl | <dl | <dl | <dl | <dl | <dl |
| **Zn** | -0.1 | -0.1 | 1.0 | -0.1 | -0.3 | -0.3 | -0.1 | 0.1 | -0.1 | 0.2 | -0.1 | -0.2 |
| **As** | 0.0 | 0.0 | 0.0 | 1.0 | -0.1 | 0.1 | 0.4 | 0.2 | 0.4 | 0.0 | **0.6** | 0.2 |
| **Se** | 0.3 | 0.0 | -0.2 | 0.4 | 1.0 | 0.3 | 0.1 | 0.0 | -0.1 | -0.2 | 0.1 | 0.3 |
| **Mo** | <dl | <dl | <dl | <dl | <dl | 1.0 | 0.0 | 0.1 | 0.0 | *0.1* | 0.0 | 0.0 |
| **Ag** | -0.1 | 0.4 | 0.0 | 0.0 | 0.1 | <dl | 1.0 | **0.6** | 0.4 | 0.0 | **0.8** | 0.4 |
| **Sb** | -0.1 | 0.0 | 0.3 | 0.1 | -0.1 | <dl | 0.2 | 1.0 | 0.5 | 0.0 | 0.3 | 0.5 |
| **Te** | -0.1 | 0.3 | 0.2 | 0.0 | -0.1 | <dl | 0.5 | **0.7** | 1.0 | 0.0 | 0.4 | 0.4 |
| **Re** | -0.1 | -0.1 | -0.1 | -0.1 | 0.0 | <dl | 0.4 | -0.1 | -0.1 | 1.0 | 0.0 | -0.2 |
| **Au** | -0.1 | 0.3 | -0.1 | **0.6** | 0.4 | <dl | **0.6** | 0.0 | 0.3 | 0.1 | 1.0 | 0.3 |
| **Bi** | -0.1 | 0.5 | 0.0 | 0.0 | 0.0 | <dl | 0.5 | 0.1 | **0.7** | -0.1 | **0.6** | 1.0 |

Fig. 9. Correlation matrix for laser ablation-inductively coupled plasma-mass spectrometry (LA-ICP-MS) analyses of molybdenite (top half) and pyrite samples (bottom half, shaded gray) from Muratdere showing the Pearson correlation coefficients of the elements. Elements with Pearson coefficients >0.6 are in bold. Abbreviation: dl = detection limit.

The two generations of molybdenite present in Muratdere—the early spherical microfracture-hosted molybdenite and the later bladed V3-hosted molybdenite (Fig. 5)—have different trace element concentrations, most notably of Re (Table 1, Fig. 8A). The spherical molybdenite crystals have a mean of 566 ppm Re ($\sigma$ = 423 ppm, n = 28), whereas the bladed molybdenite crystals contain a mean of 1,124 ppm Re ($\sigma$ = 730 ppm, n = 43, Fig. 8A). A Kolmogorov-Smirnov test was applied to establish if the distributions of the two molybdenite datasets are different. The null hypothesis was rejected as $P < 0.05$ ($P$ = 0.000122, App. 4), showing the samples to have significantly different distributions. The distribution of both populations is similar and is consistent with a log-normal distribution, with the difference in distribution being caused by location shift (i.e., different mean and median values). The bladed molybdenite has a geometric mean of 931.6 and multiplicative standard deviation of 2.003 ($P$ = 0.87), while spherical molybdenite has a geometric mean of 476.4 and multiplicative standard deviation of 2.043 ($P$ = 0.63). A nonparametric Mann-Whitney-Wilcoxian (MWW) test was then used to establish if the Re contents of the two types of molybdenite were significantly different. The median Re contents of the spherical and bladed molybdenite were 484 and 936 ppm, respectively, and, as $P < 0.05$, the null hypothesis was rejected, indicating the Re concentration of the two populations differs significantly ($U$ = 256, $n_1$ = 43, $n_2$ = 28, $P$ = 0.00001, two-tailed). Although the MWW test can produce false rejections if population distributions are different shapes, this has been shown to only be the case for log-normal distributions where standard deviations are significantly different (Fagerland, 2012), which is not the case here. These statistical tests therefore show that the spherical and bladed molybdenite have significantly different Re concentrations with a confidence of greater than 99%.

In cases where multiple analyses were carried out on the same molybdenite crystal, a large range of Re concentration was recorded, commonly showing up to an order of magnitude difference (App. 3). The bladed molybdenite crystals have ranges of 416 to 4,001 ppm Re (n = 3), and 311 to 1,364 ppm Re (n = 6) within two of the crystals analyzed. This Re heterogeneity within single crystals has been reported in other porphyry deposits (e.g., Ciobanu et al., 2013). The Re concentration in the spherical molybdenite crystals is more consistent, with ranges of 285 to 484 ppm (n = 3) and 498 to 527 ppm (n = 2) within the same crystal (App. 3).

*Trace elements in pyrite samples:* The pyrite samples analyzed from Muratdere contain <10 ppm Te, Bi, and Ag, 10 to 100 ppm Sb, As, and Se, and 100 to 1,000 ppm Co and Zn. Ni, Cu, Au, and Pb are all <1 ppm or below detection limit. Muratdere pyrite samples have mean concentrations (n = 47, Table 1, full results in App. 3) of 439 ppm Co ($\sigma$ = 1,173), 411 ppm Zn ($\sigma$ = 1,120), 108 ppm As ($\sigma$ = 375), 59 ppm Se ($\sigma$ = 38), 6 ppm Ag ($\sigma$ = 13), 12 ppm Sb ($\sigma$ = 54), 5 ppm Te ($\sigma$ = 7), and 6 ppm Bi ($\sigma$ = 14). Au and As correlate in Muratdere pyrite samples (Pearson = 0.6), as do Au and Ag (Pearson = 0.6), Te and Sb (Pearson = 0.7), and Bi and Te (Pearson = 0.7, Fig. 9). From the laser ablation trace element data, it appears that Te-Bi and Sb-Te microinclusions may be present in the pyrite as the profiles are irregular, with only limited intervals of high concentrations of elements (App. 2).

The pyrite samples in Muratdere show differences in trace element composition between vein sets (Table 1). Vein set V3 has higher Co (mean 769 ppm, n = 23) than vein sets V2 (mean 120 ppm, n = 14) and V5 (mean 122 ppm, n = 10). This difference in Co is significant according to the MWW test, meaning that V3 pyrite samples contain, on average, significantly more Co than V2 and V5 pyrite samples with a confidence of >95% ($U$ = 235.5, $n_1$ = 24, $n_2$ = 23, $P$ = 0.395, two-tailed). However, vein set V3 also contains the largest range in Co concentrations, ranging from below detection limit to 0.7 wt % Co. Vein set V3 also has significantly higher As concentrations (mean 201 ppm) than V2 (mean 32 ppm) and V5 (mean 5 ppm). Vein set V5 pyrite samples contain notably less Zn (mean 225 ppm) than vein sets V2 (mean 454 ppm) and V3 (mean 469 ppm), probably because V5 pyrite samples are in equilibrium with sphalerite.

### *EPMA of molybdenite crystals*

EPMA was used to determine the distribution of Re in three of the bladed, V3-hosted molybdenite crystals analyzed with LA-ICP-MS (Fig. 7A). They show that Re is distributed heterogeneously throughout the crystals. This produces irregular zoning, similar to that observed in other porphyry deposits (Voudouris et al., 2009; Ciobanu et al., 2013; Grabezhev and Voudouris, 2014). The zoning is best developed parallel to the cleavage, and is well preserved, with no evidence of remobilization. The high-Re zones are 10 to 20 $\mu$m thick and comprise <5 to 10% of the crystal surface area (Fig. 7A).

### *Molybdenite polytypes and microinclusions*

Bulk samples of the two generations of molybdenite were analyzed using XRD to determine their polytype. Both the early, Re-poor, microfracture-hosted molybdenite and the later, Re-rich, vein-hosted molybdenite are the 2H polytype. A high-resolution SEM survey (resolving features down to 10 nm) of molybdenite crystals was completed to ascertain the presence of microinclusions in molybdenite crystals, as has been reported in many other deposits (e.g., Hilltop, Ciobanu et al., 2013; Kalmakyr, Pašava et al., 2010). Microinclusions of galena and monazite (Fig. 7B-D) ranging from 0.5 to 5 $\mu$m

were found within bladed molybdenite crystals; however, no other microinclusions were observed.

*Stable isotopes*

*S isotopes:* The Muratdere $\delta^{34}S$ sulfide values range between –5.5 and +8.9‰, with an average of 2‰. The $\delta^{34}S$ values for anhydrites range between 12.6 and 20.3‰, typically averaging 19.0‰ (±0.8‰, 1$\sigma$; n = 6), with the exception of one sample (MDD 33 194.2), which averages 12.8‰ (n = 2). Barite averages 17.6‰ (±1.1‰, 1$\sigma$; n = 4; Fig. 10B, Table 2, full results App. 5).

Discriminating sulfide $\delta^{34}S$ values using the mineral and vein paragenesis established for the deposit shows that the microfracture-hosted sulfides (chalcopyrite-pyrite-molybdenite) have a $\delta^{34}S$ range of –2.2 to +4.2‰ (mean of 2.6 ± 1.8‰, 1$\sigma$, n = 11, Fig. 10B), whereas the earliest mineralized vein set (V2) has $\delta^{34}S$ values of sulfides (pyrite-chalcopyrite) ranging from 1.9 to 6.3‰ (mean of 4.4 ± 1.8‰, 1$\sigma$, n = 4). Sulfides (chalcopyrite-pyrite-molybdenite) in the V3 veins have a $\delta^{34}S$ range of 5.6 to 8.9‰ (mean of 7.5 ± 1.5‰, 1$\sigma$, n = 5). These data suggest a systematic increase in $\delta^{34}S$ values with progressively younger generations of veins. However, this trend is reversed for the polymetallic vein set, V5, which has sulfide (pyrite-chalcopyrite-galena-sphalerite) $\delta^{34}S$ values between –5.5 and +3.1‰ (mean of –0.4 ± 3‰, 1$\sigma$, n = 15), showing a relative decrease. Discriminating the sulfate results by vein set shows that the barite in V5 has $\delta^{34}S$ values of 16.6 to 19.2‰ (mean of 17.6‰). V6, the first anhydrite vein set, has anhydrite $\delta^{34}S$ values of 12.6 to 18.4‰ (mean of 15.5‰), and V7, the final anhydrite vein set, has $\delta^{34}S$ values of 18.7 to 20.3‰ (mean of 19.4‰, Fig. 10B, Table 2).

*Oxygen and hydrogen isotopes:* The oxygen isotope compositions for Muratdere range from 7.5 to 12.3‰ (overall mean of 9.2 ± 1.4‰, 1$\sigma$, n = 10; Fig. 10A). Microfracture and V1 to V4 quartz depicts a limited range of $\delta^{18}O$ values from 7.5 to 9.6‰ (mean of 8.7 ± 0.9‰, 1$\sigma$, n = 8). However, V5 has higher $\delta^{18}O$ values, ranging from 10.4 to 12.3‰ (mean of 11.4‰, n = 2; Table 2, Fig. 10A). Hydrogen isotope compositions from Muratdere show a narrow range from –70 to –75‰ with a mean of –73‰ (n = 6; Table 2).

## Discussion

*Mineralization conditions of the Muratdere deposit*

The Muratdere deposit is hosted by a granodioritic stock intruded into ophiolitic country rocks, including peridotite. The main mineralization is situated in hydrothermal vein sets, which are interpreted to be genetically related to later quartz-feldspar porphyry stocks. These have probably intruded from a deeper source pluton, as suggested in models for porphyry deposit formation (Sillitoe, 2010). As these stocks ascended through the crust, they exsolved volatiles, creating the hydrothermal veining observed (Cloos, 2001).

The Muratdere deposit formed through several stages of fluid-rock interaction, as evidenced by the crosscutting vein sets and overprinting alteration zones. The early vein sets, V1,

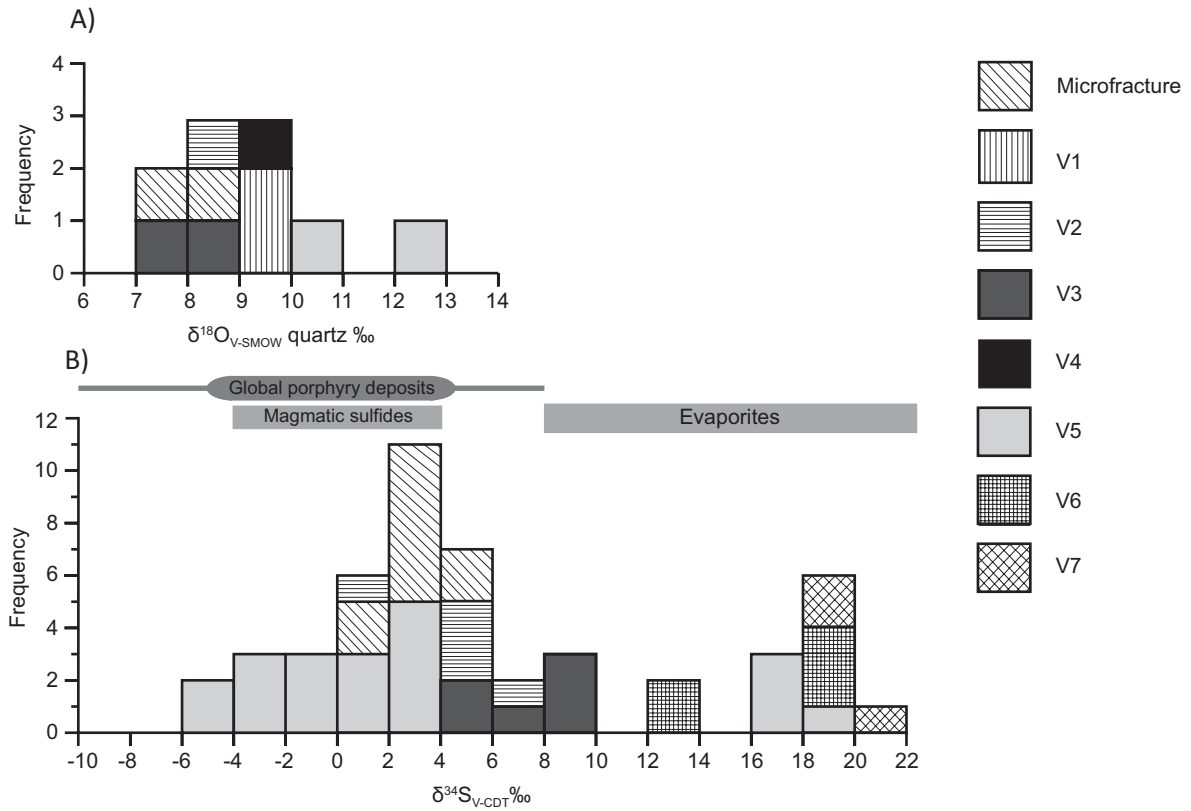


Fig. 10. A) Histogram of $\delta^{18}O_{V\text{-}SMOW}$ quartz results, discriminated by vein set. B) Histogram of $\delta^{34}S_{CDT}$ results for sulfides (microfracture, V2, V3, V5) and sulfates (V5 > 12‰, V6, V7). Global porphyry sulfide values (Hattori and Keith, 2001), magmatic sulfide values, and evaporite sulfate values (Ohmoto, 1972) are included for comparison purposes. V-CDT = Vienna-Canyon Diablo Troilite, V-SMOW = Vienna-Standard Mean Ocean Water.

Table 2. Summary of Stable Isotope Results Sorted by Mineralization Stage

| Drill hole | Depth (m) | Main vein set | $\delta^{18}O_{SMOW}$ quartz | $\delta D$ | $\delta^{34}S_{CDT}$ sulfide (av) | $\delta^{34}S_{CDT}$ sulfide (min) | $\delta^{34}S_{CDT}$ sulfide (max) | $\delta^{34}S_{CDT}$ sulfate |
|---|---|---|---|---|---|---|---|---|
| MDD 01 | 42.9 | Microfracturing | 8.8 | | 1.1 | | | |
| MDD 01 | 127.7 | Microfracturing | | | 3.1 | | | |
| MDD 03 | 142.1 | Microfracturing | 7.5 | | 4.2 | | | |
| MDD 15 | 68.2 | Microfracturing | | | 2.3 | 1.9 | 2.6 | |
| MDD 19 | 85.7 | Microfracturing | | | 3 | | | |
| MDD 24 | 49.5 | Microfracturing | | | 3.5 | 2.7 | 3.9 | |
| MDD 33 | 177.6 | Microfracturing | | | –2.2 | | | |
| MDD 03 | 112.1 | Microfracturing/V7 | | | 4 | | | 19.4 |
| MDD 24 | 86.1 | V1 | 9.6 | | | | | |
| MDD 22 | 119.7 | V1/V4 | 9.6 | | | | | |
| MDD 03 | 12.45 | V2 | | | 4.7 | | | |
| MDD 03 | 230.3 | V2 | | | 4.6 | | | |
| MDD 15 | 29.8 | V2 | | –72 | 6.3 | | | |
| MDD 33 | 55.5 | V2 | | | 1.87 | | | |
| MDD 33 | 74.6 | V2 | | | | | | |
| MDD 33 | 125 | V2 | 8.5 | –74 | | | | |
| MDD 33 | 118 | V3 | 8.6 | | 6.9 | 5.6 | 8.2 | |
| MDD 33 | 155.7 | V3 | 7.6 | –73 | 7.9 | 6.3 | 8.9 | |
| MDD 24 | 86.1 | V4 | 9.6 | –74 | | | | |
| MDD 10 | 70.25 | V5 | | | 1.8 | 0.4 | 2.7 | |
| MDD 15 | 39.2 | V5 | 10.4 | –70 | –1.5 | –5.5 | 3.1 | 17 |
| MDD 22 | 133.9 | V5 | | | –0.6 | –4 | 2.1 | |
| MDD 24 | 109.1 | V5 | 12.3 | –75 | 1.3 | | | 18.3 |
| MDD 33 | 185 | V6 | | | | | | 18.2 |
| MDD 33 | 194.2 | V6 | | | | | | 12.8 |
| MDD 33 | 165.1 | V7 | | | | | | 20.3 |
| MDD 33 | 165.1 | V7 | | | | | | 19.4 |

Note: All $\delta^{18}O$, $\delta D$, and sulfate $\delta^{34}S$ values (‰) with average (av), maximum (max), and minimum (min) $\delta^{34}S$ sulfide values
Abbreviations: CDT = Canyon Diablo Troilite, SMOW = Standard Mean Ocean Water

V2, and V3, are associated with the majority of the mineralization. Vein set V5 contains a very different metal tenor (Fig. 6), including relatively high concentrations of Pb and Zn, which are not present in such high concentrations elsewhere in the deposit. V2 and V3 are associated with potassic alteration and magnetite, whereas V4 and V5 are associated with chlorite-sericite alteration and hematite. The transition between magnetite and hematite in the alteration assemblages between vein sets V4 and V5 shows an increase in the oxygen fugacity of the system. This is consistent with the presence of barite in V5 and anhydrite in V6 and V7, indicating an increase in $SO_4/H_2S$ throughout the paragenesis from an $H_2S$-dominated environment in V1 to V3 to a, $SO_4$-dominated system in V5, V6, and V7. V6 and V7 veins are also associated with a late advanced argillic overprint, signified by kaolinite and pyrophyllite, and this reflects the transition toward more acidic, high-sulfidation conditions.

*Oxygen and hydrogen isotopes:* The oxygen and hydrogen isotope results recorded at Muratdere are very similar to the values for porphyry deposits globally; for example, quartz from veins in the Bingham deposit, Utah, show $\delta^{18}O$ values of 8.6 to 9‰ and $\delta D$ values of –69 to –83‰ (Sheppard et al., 1971; Sheppard and Gustafson, 1976; Ford and Green, 1977; Bowman et al., 1987; Zaluski et al., 1994). The vein sets from Muratdere have an extraordinarily narrow $\delta D$ range, with all vein sets being within error of the deposit average of –73‰. This is unusual; however, meteoric water in Anatolia in the Eocene had a $\delta^{18}O$ value of approximately –10‰ and a $\delta D$ value of approximately –75‰ (Giggenbach, 1992; Imbach, 1997; Bowen and Wilkinson, 2002), which is within the range of magmatic $\delta D$. This means that any input of a new meteoric (or magmatic) fluid source would not necessarily be recorded in the $\delta D$ values of the ore-forming fluid—only in the $\delta^{18}O$ values.

The $\delta^{18}O_{H_2O}$ values of ore-forming fluids from quartz were calculated using the equation $1{,}000\ln\alpha_{quartz\text{-}H_2O} = 3.38 \times 10^6 T^{-2} - 3.40$ (Clayton et al., 1972). The temperatures used for vein sets V1 to V3 were calculated from the in situ $\delta^{34}S$ values of chalcopyrite and pyrite crystals that appear to be in equilibrium, using the equation of Kajiwara and Krouse (1971). This gave an average temperature for V3 of 528°C. This temperature is consistent with the temperatures of fluids associated with potassic alteration in porphyry deposits globally (Sillitoe, 2010; Bodnar et al., 2013), and so was used as an approximate temperature for calculating the $\delta^{18}O_{H_2O}$ values of V1 to V3, all of which are associated with potassic alteration. $\delta^{18}O_{H_2O}$ values were also calculated for the maximum and minimum temperatures of fluid inclusions associated with potassic alteration zones in porphyry deposits (600° and 200°C, respectively, from the global compilation in Bodnar et al., 2013) to give a range of $\delta^{18}O_{H_2O}$ error and represent the possible spread if the veins were at different temperatures (Fig. 11). The temperature for vein set V5 was calculated from the in situ $\delta^{34}S$ values of galena and pyrite crystals that appear to be in equilibrium, using the equation of Ohmoto and Rye (1979). This gave an average temperature for V5 of 378°C, which is consistent with chlorite-sericite alteration, and so this was used as the approximate temperature for vein sets V4 and V5, both of which are associated with chlorite-sericite alteration. As for V1 to V3, maximum and minimum global porphyry deposit temperatures from fluid inclusions in similar alteration zones

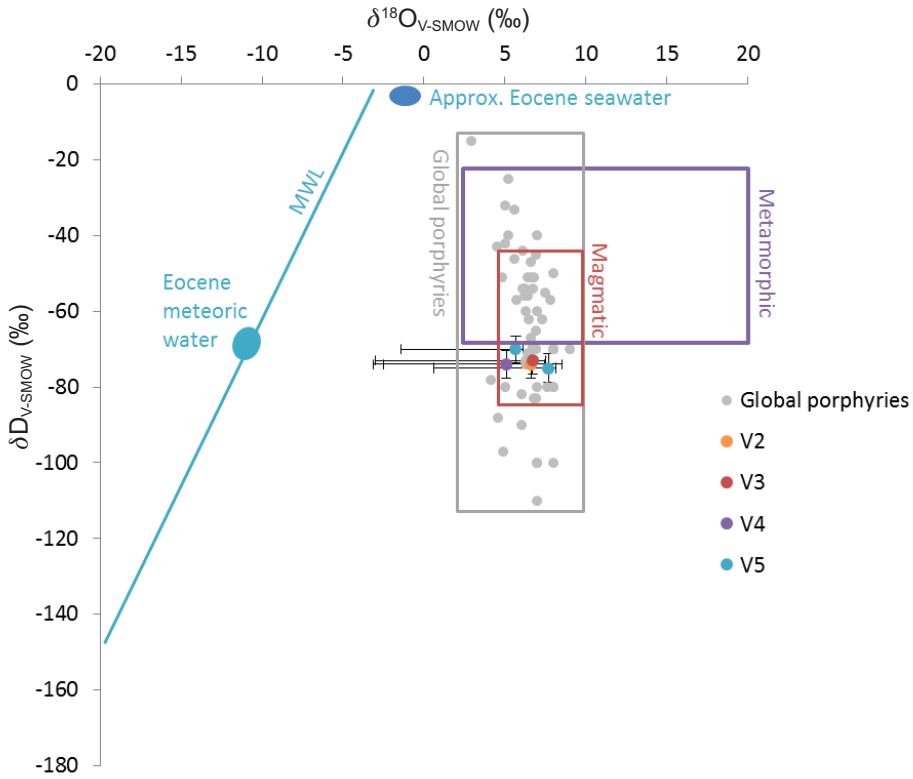


Fig. 11. Fluid oxygen isotope compositions versus hydrogen isotope compositions for Muratdere compared with global porphyries (MWL = meteoric water line). Fluid $\delta^{18}O$ values calculated according to equation from Matsuhisa et al. (1979). Error bars in $\delta^{18}O$ values represent the range of temperatures for global porphyry fluid inclusions associated with the alteration style of each vein set from the global compilation in Bodnar et al. (2013), while those on $\delta D$ values represent analytical error. Magmatic, metamorphic, and meteoric water values (calculated for Turkey during the Eocene) from Taylor and Sheppard (1986), and global porphyry fluid data from Sheppard et al. (1971), Sheppard and Gustafson (1976), Ford and Green (1977), Bowman et al. (1987), and Zaluski et al. (1994). V-SMOW = Vienna-Standard Mean Ocean Water.

(400° and 200°C; Bodnar et al., 2013) were used to calculate the error of $\delta^{18}O_{H_2O}$ values for vein sets V4 and V5. These temperature ranges give a large uncertainty in $\delta^{18}O_{H_2O}$ values; however, we note that fluid oxygen and hydrogen isotope data from Muratdere plot in the global porphyry field (Fig. 11, Sheppard et al., 1971; Sheppard and Gustafson, 1976; Ford and Green, 1977; Bowman et al., 1987; Zaluski et al., 1994) and are likely to be magmatic.

*Sulfur isotopes:* The average sulfide $\delta^{34}S$ value for Muratdere is +2‰, which is similar to that of many other porphyry deposits and is within the upper end of the range for magmatic sulfur (Ohmoto, 1972). However, sulfides from the Muratdere deposit display a wide range of $\delta^{34}S$ values compared to sulfides in porphyry deposits globally (Figs. 10, 12; Hattori and Keith, 2001). The majority of porphyry Cu deposits do not exceed $\delta^{34}S_{CDT}$ values of ~4‰, whereas the highest $\delta^{34}S$ value recorded from Muratdere is 8.9‰. The range of $\delta^{34}S$ values at Muratdere is mostly similar to those seen at Cerro Verde-Santa Rosa in Peru (Eastoe, 1983). Whole-rock sulfur extracts from other postcollisional granitoids in central Anatolia also show high $\delta^{34}S$ values, averaging between 3.3 and 13.2‰ (Boztug and Arehart, 2007), and this is thought to be due to crustal contamination during magma-crust interaction or the assimilation of sulfate.

While the bulk of Muratdere values fall within a local magmatic S isotope range, there is a significant variation in $\delta^{34}S$ values through the paragenesis (Fig. 12A). The microfracture-hosted sulfides and sulfides from V2 show a strong magmatic $\delta^{34}S$ signature, corresponding to a melt source. The sulfides in the Re-rich, molybdenite-bearing V3 have higher $\delta^{34}S$ values than any earlier mineralizing events in Muratdere, and V3 molybdenite samples have the highest $\delta^{34}S$ values of the sulfides (8.2–8.8‰). These values are significantly higher than the $\delta^{34}S$ values of the early microfracture-hosted chalcopyrite and molybdenite samples (Fig. 13A). This is in contrast to results from porphyry systems in Russia and Mongolia (Berzina et al., 2005), where the $\delta^{34}S$ values of molybdenite samples in Re-enriched deposits (Aksug and Erdenetuin-Obo) are close to mantle compositions (–0.9 to +3.2‰), whereas the $\delta^{34}S$ values for molybdenite from Re-poor deposits (Zhireken, Shatkhtama, and Sora) are higher, ranging from 3.7 to 10.2‰ (Fig. 12B).

The higher $\delta^{34}S$ values of V3, as opposed to those in V2, suggest either that a new sulfur source became available at this point in the paragenesis or that these increasing values are part of an overall fractionation trend toward higher $\delta^{34}S$ values. Given the oxidizing trend from the early to late veins and the increase in $SO_4/H_2S$ throughout the paragenesis of the deposit, it is likely that this change in redox conditions is responsible (Seal, 2006). Vein set V5, however, has lower $\delta^{34}S$ values, with a mean sulfide $\delta^{34}S$ value of –0.4‰, which contrasts with the general trend of increasing sulfide $\delta^{34}S$ values

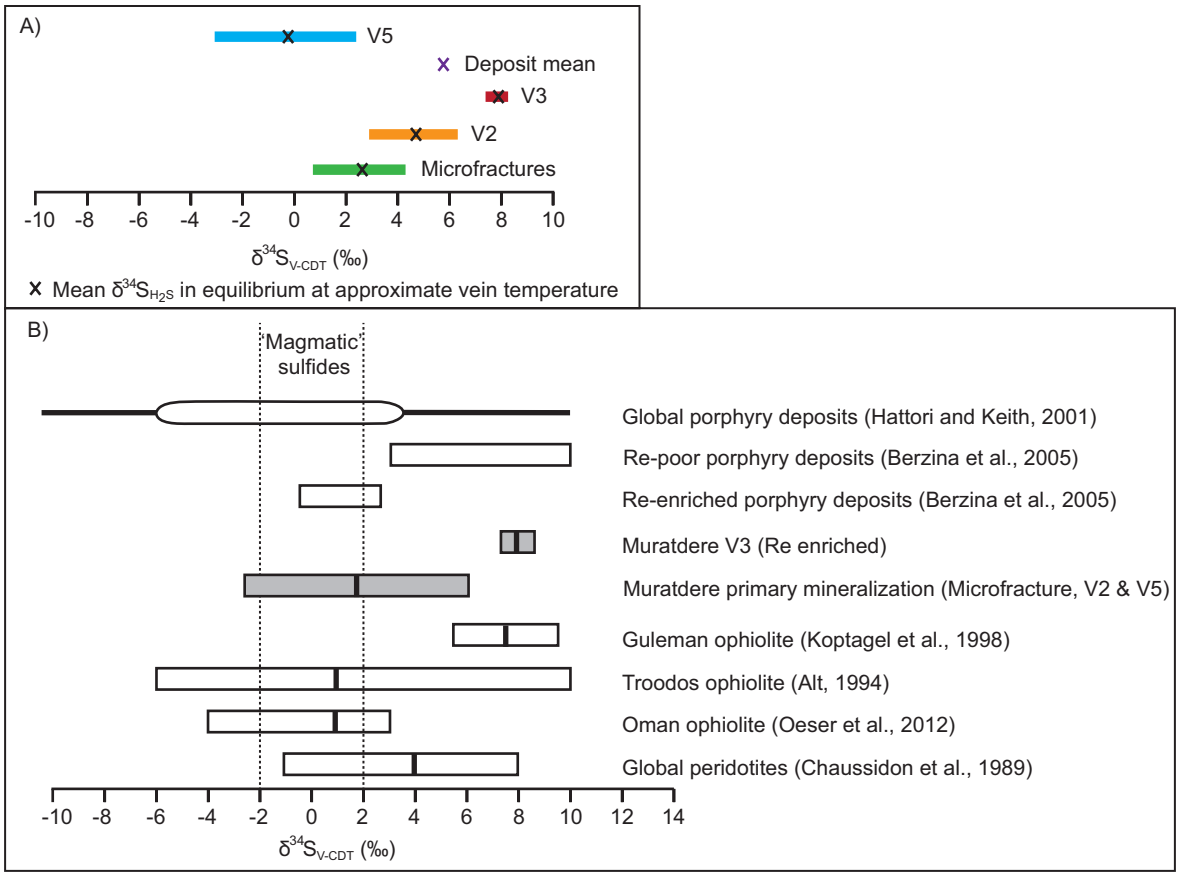


Fig. 12. A) Variation of $H_2S$ $\delta^{34}S$ values with vein set showing the changes in $\delta^{34}S_{H_2S}$ values over time. The $\delta^{34}S_{H_2S}$ values at equilibrium were calculated using the estimated temperatures for the vein sets from sulfur isotope equilibria calculations and so are approximate; however, the difference between maximum and minimum temperature for each system is only 0.1‰ (equations used: pyrite-$H_2S$, molybdenite-$H_2S$, and sphalerite-$H_2S$, Ohmoto and Rye, 1979; chalcopyrite-$H_2S$ and galena-$H_2S$, Li and Liu, 2006). B) Diagram showing the range of and mean $\delta^{34}S$ values for a variety of ophiolites and porphyry deposits, with the mean represented by a line in the center of the box (Ohmoto, 1972; Chaussidon et al., 1989; Alt, 1994; Koptagel et al., 1998; Berzina et al., 2005; Oeser et al., 2012). The gray shaded boxes represent the $\delta^{34}S$ values from this study; the "Re-enriched porphyry deposits" are the Aksug and Erdenetuin-Obo deposits in Russia and Mongolia; and the "Re-poor" porphyry deposits are Zhireken, Shatkhtama, and Sora from Russia and Mongolia (Berzina et al., 2005). V-CDT = Vienna-Canyon Diablo Troilite.

(Fig. 12A), although this may be due to disproportionation of $SO_4$ (Rye, 1993).

Alternatively, or additionally, a new source of sulfur may have become available. $\delta^{34}S$ data from the Guleman Group in southeastern Anatolia, a Late Cretaceous ophiolite similar to the Dağküplü ophiolite, show relatively high $\delta^{34}S$ values of 5.8 to 8.8‰ (Koptagel et al., 1998), which match the $\delta^{34}S$ values of the V3 veins (5.6–8.9‰). These values are higher than the $\delta^{34}S$ values recorded in the Oman ophiolite (–2 to +4.4‰; Oeser et al., 2012), but are within the values recorded for peridotites globally (Chaussidon et al., 1989) and in the Troodos ophiolite (–1.9 to +10.8‰; Fig. 12B; Alt, 1994). This suggests the surrounding Dağküplü ophiolite could be a viable source of sulfur derived through hydrothermal fluids scavenging sulfur and metals from the surrounding country rock, as the temperatures of felsic magmas are lower than those needed to fully assimilate the peridotite country rock (Ito and Kennedy, 1967).

While the $\delta^{34}S$ values of sulfates in Muratdere are broadly within the expected range for Eocene seawater sulfate, which is 16 to 23‰ (Thode and Monster, 1965; Claypool et al., 1980), we note that there is no suggestion of marine influence in the earlier H data. The sulfates in Muratdere are more likely to be magmatic, with the higher $\delta^{34}S$ values occurring due to the temperature of precipitation in a system with significant $H_2S$ during disproportionation (Rye, 2005).

### *Trace elements in molybdenite*

*Rhenium hosting in molybdenite:* The average Re content of molybdenite crystals in Muratdere (904 ppm) is above the range and average Re content of molybdenite in porphyry deposits globally (690 ppm) and is similar to the average Re in molybdenite values reported for the Skouries and Maronia deposits, Greece, the Kalmakyr deposit, Kazakhstan, and the San Manuel deposit, Arizona (data from Berzina et al., 2005; Singer et al., 2005; Grabezhev, 2007; Pašava et al., 2010; Ciobanu et al., 2013; Grabezhev and Voudouris, 2014; Fig. 8C). Muratdere contains two Re-bearing phases—early, microfracture-hosted molybdenite and later, V3 vein-hosted molybdenite. The later, vein-hosted molybdenite crystals in V3 contain

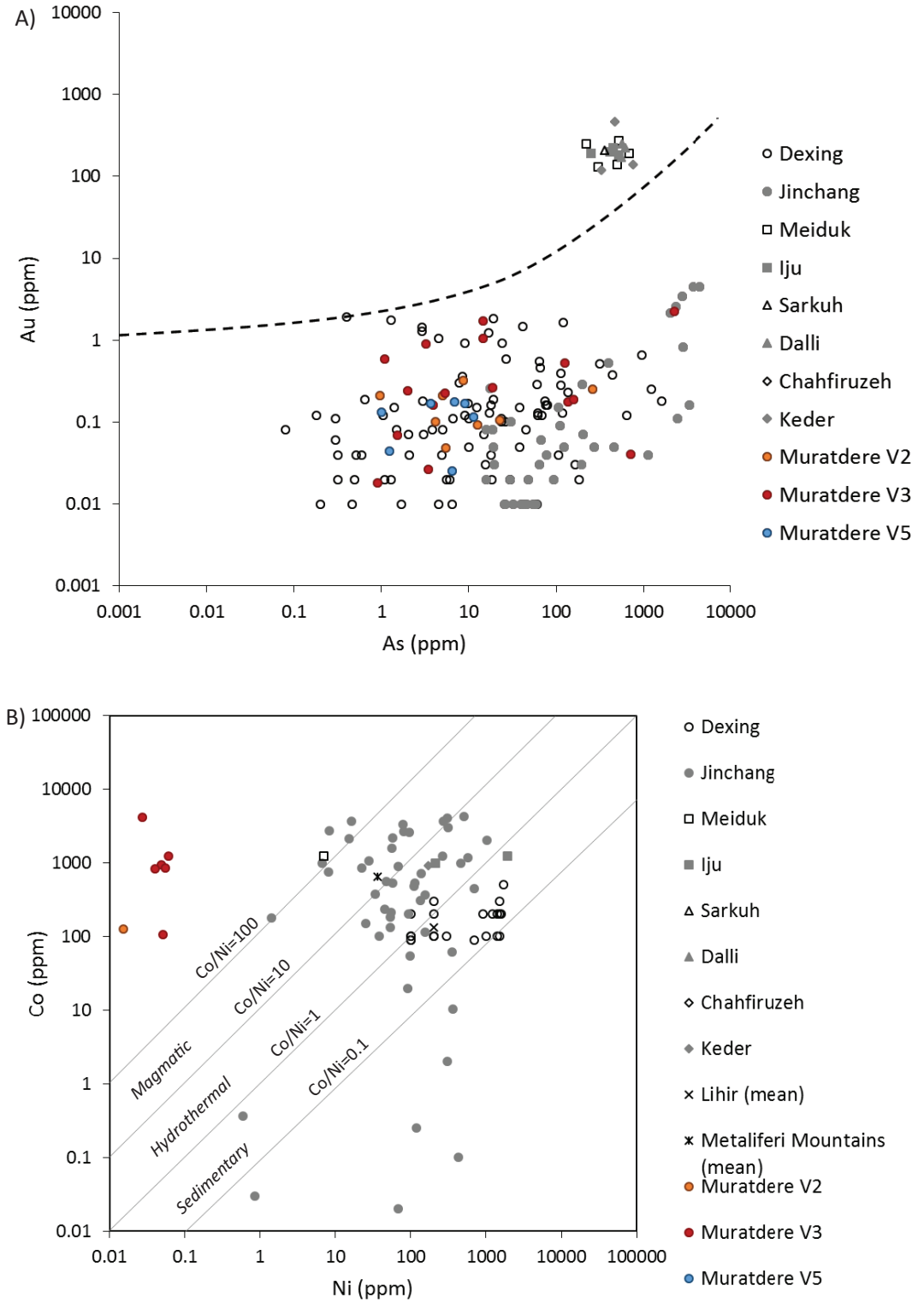


Fig. 13. Laser ablation-inductively coupled plasma-mass spectrometry (LA-ICP-MS) analyses of pyrite crystals from Muratdere discriminated by vein set and compared to LA-ICP-MS analyses of pyrite samples from global porphyry deposits (data from Reich et al., 2013; Cioacă et al., 2014; Zhang et al., 2016; Sykora et al., 2018; Zarasvandi et al., 2018). A) Au against As in global porphyry pyrite samples (where both are above detection limit). The black dashed line represents the solubility limit for Au solid solution as a function of As after Reich et al. (2013). Pyrite samples plotting above the line host Au as $Au^0$ in nanoinclusions, while below the line Au is hosted as $Au^{1+}$ in Au-As solid solution. B) Co and Ni concentrations of pyrite samples from global porphyries (where above detection limit). Co/Ni lines and labeled fields represent the provenance indicators suggested by Bralia et al. (1979), with values above 10 suggested to indicate magmatic, 1 to 10 hydrothermal, and <1 sedimentary origin.

significantly more Re than the early microfracture-hosted molybdenite crystals. Previous studies have also reported differences in Re content between different molybdenite generations. For example, the Cadia Quarry Au-Cu porphyry, Australia, and the Sar Cheshmeh Cu-Mo porphyry, Iran, also have two generations of molybdenite, with later molybdenite crystals being richer in Re than the early samples (Wilson et al., 2007; Aminzadeh et al., 2011), while in the Boddington Au-Cu porphyry, Australia, and the El Teniente Cu-Mo porphyry, USA, it is the early molybdenite samples that are relatively enriched in Re (Stein et al., 2001a; Spencer et al., 2015).

Heterogeneous distribution of Re within molybdenite is observed in many porphyry deposits. Large ranges in Re concentrations across single molybdenite crystals are reported at the highly Re enriched Pagoni Rachi deposit, Greece, and the Re-enriched Vosnesensk deposit, Russia (Voudouris et al., 2009; Grabezhev and Voudouris, 2014). Oscillatory zoning of Re is commonly observed within individual molybdenite crystals and has been suggested to indicate that successive hydrothermal events with different Re contents may occur in porphyry deposits (Ciobanu et al., 2013). However, irregular zoning, as is present in the bladed molybdenite of Muratdere (Fig. 7A), has been suggested to represent the original growth pattern of the crystals (Grabezhev and Voudouris, 2014).

The Re-rich molybdenite in Muratdere is of the 2H polytype, as are those at Pagoni Rachi, Hilltop, and Vosnesensk (Voudouris et al., 2009; Ciobanu et al., 2013; Grabezhev and Voudouris, 2014). It is unknown how polytype affects Re concentrations in molybdenite. Theoretically, the crystal structure of the 3R polytype should accommodate more impurities, which could include Re, and so a relationship between the Re concentration and the amount of 3R molybdenite in porphyry deposits has been proposed (Newberry, 1979). Both the 2H to 3R polytype ratio of molybdenite and the abundance of Re in molybdenite have also been suggested to increase over time during the potassic alteration phase (Newberry, 1979). However, Voudouris et al. (2009) concluded that high Re concentrations are due to isovalent Re substitution for Mo in molybdenite and are not affected by polytype, which is supported by the lack of the 3R polytype in Muratdere.

*Other trace elements in molybdenite:* Selenium has been suggested to be incorporated into molybdenite via isometric substitution, as $MoSe_2$ is isostructural with $MoS_2$ and so $Se^{2-}$ may substitute for $S^{2-}$ in the lattice (Drábek, 1995; Ciobanu et al., 2013; Pasava et al., 2016). The two generations of molybdenite in Muratdere both contain Se, with very consistent concentrations and flat TRA profiles (App. 2). The other trace elements observed in molybdenite in Muratdere are less consistent, with very variable concentrations between and within molybdenite crystals. Although, theoretically, $Te^{2-}$ could substitute for $S^{2-}$ in molybdenite (Drábek, 1995; Pasava et al., 2016), the Te concentrations in Muratdere molybdenite crystals are very variable, and TRA profiles show irregular patterns that have been suggested to show the presence of micro- or nanoinclusions (Ciobanu et al., 2013; Pasava et al., 2016). Te and Bi correlate in the bladed molybdenite, which may imply the presence of bismuth-tellurium mineral microinclusions, as observed at Kalmakyr (Pasava et al., 2016). Although a high-resolution SEM survey of the bladed molybdenite crystals in Muratdere showed the presence of only galena microphases (Fig. 7B), with no Te- or Bi-bearing phases observed, irregular TRA profiles from LA-ICP-MS suggest the presence of inclusions (App. 2). Due to their chalcogenide affinity if Te and Bi are present in molybdenite, this is suggested to attract Ag and Au incorporation, generally as inclusions of precious metal-semimetal minerals (Ciobanu et al., 2013). This is observed at the Hilltop deposit, where Te, Bi, and Pb are associated with Au and Ag, and at Kalmakyr where Au-Bi inclusions are observed (Ciobanu et al., 2013; Pasava et al., 2016). Although precious metal-bearing mineral inclusions were not observed in Muratdere molybdenite samples, all LA-ICP-MS analyses with Au >0.2 ppm and Ag >1 ppm also contain Te and Bi concentrations of >1 ppm, and there is a positive correlation between Te + Bi and Au + Ag (Fig. 8B). Co, As, Zn, and Sb also appear to be present as inclusions due to their highly variable concentrations and uneven TRA profiles.

Molybdenite crystals in Muratdere contain Se, Co, As, Ag, Sb, and Bi concentrations similar to those analyzed from the Kalmakyr deposit, Kazakhstan (Pašava et al., 2010), with higher Te and Au concentrations. The Hilltop molybdenite samples, however, contain higher concentrations of trace elements than those from Muratdere (Ciobanu et al., 2013). Although galena microinclusions were observed in Muratdere molybdenite crystals, no Pb was detected in any of the molybdenite samples analyzed with LA-ICP-MS. This contrasts with Kalmakyr and Hilltop, where Pb is a significant trace element in molybdenite samples (Ciobanu et al., 2013; Pasava et al., 2016).

*Trace elements in pyrite*

Hydrothermally precipitated pyrite generally contains a large range of trace elements, with Ni, As, Co, Cu, and Sb reported in up to wt % concentrations in porphyry Cu deposits and Ag, Au, Cu, Sn, Te, Se, and Bi commonly also present (Abraitis et al., 2004; Reich et al., 2013). These trace elements are either present in the lattice as stoichiometric substitutions, such as $Co^{2+}$ and $Ni^{2+}$ for $Fe^{2+}$ or $Se^{2-}$ and possibly $Te^{2-}$ for $S^{2-}$; within the lattice as nonstoichiometric substitution, as is proposed for As; or as micro- or nanoinclusions within the sulfide (Abraitis et al., 2004; Cook et al., 2009; Winderbaum et al., 2012; Reich et al., 2013). It is likely that Te and Ag are present as inclusions in Muratdere pyrite grains due to their highly variable concentrations between pyrite crystals in the same sample and irregular TRA profiles, which are thought to indicate the presence of nano- or microinclusions (App. 2; Reich et al., 2013). Selenium and cobalt, however, have smooth TRA profiles, which suggests they are present in the lattice by substitution in Muratdere. Antimony and bismuth have irregular TRA profiles in some crystals and smooth profiles mirroring S in others, suggesting they may be present both in the lattice (likely as evenly distributed nanoinclusions) and as microinclusions (App. 2).

Muratdere has similar Ag, Sb, Zn, and Bi concentrations as pyrite samples from other porphyry deposits that have undergone sulfide trace element analysis (Reich et al., 2013; Cioacă et al., 2014; Zhang et al., 2016; Sykora et al., 2018; Zarasvandi et al., 2018). Pyrite samples from the Dexing and Jinchang porphyry deposits, China, the Lihir porphyry-epithermal deposit, Papau New Guinea, and the Muratdere deposit contain relatively similar Au and Te concentrations (<1 ppm), in contrast to pyrite samples from porphyry deposits in the Metaliferi

Mountains, Romania, and the Urumieh-Dokhtar arc, Iran, which contain significantly more Te (mean 89 and 47 ppm) and Au (mean 168 and 145 ppm) than pyrite from other porphyry deposits (Cioacă et al., 2014; Zarasvandi et al., 2018). Pyrite samples analyzed by LA-ICP-MS from the Jinchang porphyry deposit, China, have Ni and As concentrations similar to those of Muratdere pyrite samples, but with slightly more Co (mean 949 ppm) and an order of magnitude less Se present (mean 2 ppm) (Zhang et al., 2016). Pyrite samples analyzed by EPMA/secondary-ion mass spectrometry (SIMS) at the Dexing porphyry Cu-Au-Mo deposit also have similar As concentrations and contain significantly less Se (mean 6 ppm) than Muratdere, but contain an order of magnitude more Ni (mean 140 ppm, Reich et al., 2013). Pyrite samples analyzed by EPMA from porphyry deposits in the Urumieh-Dokhtar arc, Iran (the Meiduk, Iju, Sarkuh, Dalli, Chahfiruzeh, and Keder deposits), contain similar amounts of Ni, significantly more As (mean 478 ppm), slightly more Co (mean 967 ppm), and significantly less Se (mean 9 ppm) than Muratdere (Zarasvandi et al., 2018). Pyrite samples analyzed by EPMA from porphyry deposits in the Metaliferi Mountains have Co and Se contents similar to those of the Muratdere deposit, with more Ni (mean 36 ppm, n = 148) and As (mean 575 ppm, Cioacă et al., 2014), while pyrite samples from the Lihir telescoped Au porphyry-epithermal deposit contain more Se than Muratdere (mean 125 ppm) but otherwise have very similar Ni, Co, and As concentrations (Sykora et al., 2018).

Muratdere pyrite crystals have highly variable As concentrations, ranging from below detection limit to 0.2 wt %. It has been shown in other hydrothermal ore deposits that arsenian pyrite has higher trace element concentrations than As-free pyrite (e.g., Huston et al., 1995; Abraitis et al., 2004; Chouinard et al., 2005; Deditius et al., 2011; Cook et al., 2013; Reich et al., 2013; Cioacă et al., 2014). This is thought to be due to the incorporation of As into pyrite, which creates lattice defects that supply vacancies for the incorporation of trace element nanoinclusions, as well as allowing the substitution of metals with larger ionic radii, such as Au, for Fe (Abraitis et al., 2004; Chouinard et al., 2005; Reich et al., 2005; Deditius et al., 2014). In Muratdere, however, there is no correlation between As, Te, Bi, and Sb, although Au does show a positive correlation with As, with only pyrite samples with As greater than the detection limit containing any Au. This coupling of Au with As in pyrite is well known, and it has been shown that arsenic promotes the incorporation of Au in pyrite, either into the lattice as an $Au^{+}$-$As^{-}$ solid solution or as $Au^{0}$ nanoparticles (Chouinard et al., 2005; Reich et al., 2005; Cook et al., 2013). The incorporation mechanism of Au is controlled by the solubility of Au-As in pyrite, with pyrite crystals that plot above the Au-As solubility line hosting Au as nanoparticles (Reich et al., 2005; Deditius et al., 2011, 2014). Pyrite crystals from porphyry Cu deposits plot both above and below this curve (Fig. 13A, Reich et al., 2013; Cioacă et al., 2014), and so both methods of incorporation are possible. Muratdere pyrite crystals plot below the solubility curve (Fig. 13A), suggesting that Au is likely present as solid solution. However, the solubility curve was calculated for temperatures between 150° and 250°C (Reich et al., 2005) and so may be positioned differently at the higher temperatures present in porphyry copper deposit systems.

*Trace elements in pyrite as genetic indicators:* Trace element concentrations in hydrothermal pyrite samples are notoriously variable, both within deposits and even within single crystals due both to microinclusions and to trace element zoning due to changes in hydrothermal fluid conditions (Abraitis et al., 2004; Winderbaum et al., 2012; Reich et al., 2013). This weakens correlations between elements (Winderbaum et al., 2012) and makes drawing genetic conclusions from pyrite trace element chemistry unreliable. The large variability of trace element concentrations, even within vein sets at Muratdere, is therefore typical of porphyry deposits, and care should be taken when drawing broader conclusions from these data (Winderbaum et al., 2012; Reich et al., 2013; Cioacă et al., 2014; Zhang et al., 2016).

Co/Ni of pyrite samples has been proposed as a genetic provenance indicator, with large ratios (>10) thought to indicate either high temperatures or magmatic pyrite (Bralia et al., 1979; Bajwah et al., 1987; Huston et al., 1995; Zhang et al., 2016). Muratdere has very high Co/Ni values (average Co/Ni = 4,380), due to the very low Ni contents of Muratdere pyrite samples, with most pyrite crystals analyzed being below detection limit (Fig. 13B). The porphyry deposits from the Urumieh-Dokhtar arc also commonly have Ni contents below detection (Zarasvandi et al., 2018), and pyrite samples from the Jingchan and Dexing porphyry deposits show a very large range of Ni and Co values, from below detection limit to >0.1 wt %, with some pyrite samples falling in the "sedimentary" field, as defined by Bralia et al. (1979; Fig. 13B). This large heterogeneity within single deposits and even within paragenetic stages suggests that Co/Ni in porphyry deposit pyrite samples is not controlled by genetic provenance, but rather by the changing Co/Ni of the magmatic-hydrothermal fluids. Oscillatory Ni zoning has been observed within porphyry pyrite crystals, which supports the hypothesis that Ni concentration is controlled by the metal content of the mineralizing fluid (Reich et al., 2013). This means that, while Co/Ni may be of use in identifying the provenance of pyrite samples from volcanogenic massive sulfide and sedimentary exhalative deposits (Bralia et al., 1979; Bajwah et al., 1987), it is of limited use in porphyry Cu deposits.

### *Potential sources of rhenium in Muratdere*

The source of Re in porphyry deposits has generally been agreed to be from an Re-enriched source melt, either as a primary melt or secondary ultramafic input. This has been suggested to be derived from degassing of a down-going slab (Sun et al., 2003), incorporation of Re-enriched anoxic sediments into the accretionary wedge (Tessalina et al., 2008), or partial melting of previously metasomatized mantle lithosphere triggered by a local ascent of asthenospheric mantle (Voudouris, 2006; Voudouris et al., 2009). Eocene magmatism in the north of Turkey is postcollisional, with metal enrichment resulting from upwelling asthenospheric mantle melting previously metasomatized crust (Stein et al., 2001b; Berzina et al., 2005; Kuscu, 2016). This could provide an Re (and indeed Cu and Au) enrichment mechanism for Muratdere. However, this does not explain the difference in Re content between the two generations as, if the whole Re budget for a given system were sequestered into molybdenite (Stein et al., 2001b), the earlier molybdenite generations would be expected to have higher Re contents.

One possible cause of the Re enrichment seen in V3 is a change in the fluid conditions to those that better favor Re deposition. As discussed above, the fluid system at Muratdere also became more oxidized over time and, given that oxidized fluids also favor the transport of Re (Xiong and Wood, 2002), this change to more favorable oxidizing fluid conditions could explain the Re enrichment of the later molybdenite generation.

Another possibility is that a new source of Re became available between the microfracturing event and the precipitation of the V3 molybdenite. If this new Re source was a new influx of mafic or ultramafic magma into the felsic pluton (Sinclair and Jonasson, 2014), then a new intrusive phase or evidence of a change in the host porphyry composition might be expected between vein sets V2 and V3, but this is not seen. As discussed above, however, the fluids that formed vein set V3 may have scavenged isotopically $\delta^{34}$S enriched sulfur from the surrounding peridotitic country rock. This hydrothermal fluid-country rock interaction could also provide additional Re, as well as the other chalcophile elements such as Au and Cu. Ophiolites contain between 0.17 and 1.95 ppb Re (Ravizza et al., 2001; Peucker-Ehrenbrink et al., 2012; Becker and Dale, 2016), and the highly serpentinized peridotite observed at the bottom of drill hole MDD 03 has a bulk-rock Re content of 0.1 ppm (Stratex International, 2017). A rough mass balance calculation shows that it would take a volume of ~0.06 km$^3$ of ophiolite at 1 ppb Re to produce the total estimated resource of 17,594 kg Re (Stratex International, 2017), assuming all available Re was stripped out and the ophiolite has a consistent Re content. Muratdere has an alteration footprint of approximately 1.6 km$^3$, meaning that even if only 40% of that footprint was in ophiolite it could still provide enough Re to account for the whole resource. This is unlikely to be the case as the magmatic fluids would also carry Re sourced from the melt, and at least the early Re hosted in the spherical molybdenite samples is likely to be entirely magmatic. However, hydrothermal interaction between the fluid that formed the V3 vein set and the surrounding ophiolite could have "upgraded" the Re concentration of the later bladed molybdenite crystals and thus increased the Re resource of the deposit.

That said, there is no evidence of a similar consistent upgrading of other hydrothermally mobile chalcophile elements that are present in high concentrations in ophiolites, such as Ni, Pd, and Co. Molybdenite and pyrite samples from vein set V3 are the only ones to have Ni and Pd above detection limit; however, the concentrations are very low (0.06 ppm Ni and 0.8 ppm Pd), and they are only detected in five crystals. As discussed above, the pyrite crystals in V3 have a higher average Co concentration than those in V2; however, both have very large standard deviations, so this is inconclusive. While it is possible that hydrothermal interaction of late fluids with the surrounding ophiolite could be a source of additional Re (and isotopically heavy S), it is equally possible that the enrichment seen is a result of changing fluid conditions during deposit genesis.

## Conclusions

Muratdere is a postcollisional Cu-Mo (Au-Re) porphyry deposit hosted by granodiorite and quartz-feldspar porphyry stocks. The deposit contains three main vein stages: an early mineralizing stage, which is associated with potassic alteration and hosts the Cu, Mo, and Re mineralization; a porphyry-epithermal transition stage consisting of intermediate-sulfidation polymetallic veins associated with chlorite-sericite alteration that host Zn, Pb, and Au mineralization; and a late advanced argillic overprint, associated with anhydrite vein sets. The alteration types and vein sets present are similar to those seen at the highly Re enriched Pagoni Rachi deposit, Greece.

Molybdenite samples in the Muratdere deposit have Re concentrations above the global average for Cu-Mo porphyry deposits, with an average of 904 ppm Re. Muratdere contains two generations of molybdenite with significantly different Re concentrations. The earlier microfracture-hosted molybdenite contains an average Re concentration of 566 ppm and magmatic $\delta^{34}$S values which suggest that this Re is likely from an enriched melt source. This is proposed to be the result of upwelling asthenospheric mantle melting previously metasomatized crust. The later, vein-hosted molybdenite crystals in V3 contain an average of 1,124 ppm Re, which is similar to that of other Re-enriched porphyries at Kalmakyr and Copper Creek (Berzina et al., 2005). Vein set V3 has higher $\delta^{34}$S values than the other mineralized vein sets, with values near the upper end of $\delta^{34}$S values recorded in porphyries globally (Hattori and Keith, 2001) and very similar to $\delta^{34}$S recorded for Anatolian peridotites. This may suggest that there has been hydrothermal interaction of the fluids that formed vein set V3 with the surrounding ophiolite, scavenging sulfur and upgrading the Re content of the late molybdenite crystals. However, there is only a moderate enrichment in other chalcophile elements associated with ophiolites (e.g., Co, Ni, Pd, and Au) in V3, and it is perhaps more likely that the Re and heavy $\delta^{34}$S enrichment in the later molybdenite crystals is due to the changing of fluid conditions to a higher oxidation state.

## Acknowledgments

We would like to acknowledge the help of Dr. Richard Pearce and Dr. Duncan Muir for their support on the SEM at the University of Southampton and Cardiff University, respectively, Mr. John Ford and Mr. Robert Jones for thin section preparation, Mr. Ross Williams for his support on the XRD at the University of Southampton, Dr. John Spratt for his support with the EPMA at the Natural History Museum, and Mrs. Alison McDonald and Mr. Terry Donnelly for their support with the stable isotope work at SUERC. Many thanks are also due to Mr. Bahri Yildiz and the rest of the Stratex International team in Turkey for logistical support in the field and Lodos Madencilik for providing assay data. We would also like to thank Dr. Tom Gernon for his discussions on this manuscript, and Dr. Isabel Barton, Dr. Brian Rusk, and Dr. Robert Moritz for their helpful reviews. This work was funded by the University of Southampton Mayflower Scholarship and by National Environmental Research Council (NERC) SoS Consortium grant NE/M010848/1, "TeaSe: Tellurium and selenium cycling and supply," awarded to Cardiff University, and stable isotope work was funded by NERC facility grant [IP-1373-0513]. AJB is funded by NERC support of the Isotope Community Support Facility at SUERC, and JN publishes with the permission of the executive director of the British Geological Survey (NERC).

## REFERENCES


Abraitis, P.K., Pattrick, R.A.D., and Vaughan, D.J., 2004, Variations in the compositional, textural and electrical properties of natural pyrite: A review: International Journal of Mineral Processing, v. 74, p. 41–59.

Akay, E., 2009, Geology and petrology of the Simav magmatic complex (NW Anatolia) and its comparison with the Oligo-Miocene granitoids in NW Anatolia: Implications on Tertiary tectonic evolution of the region: International Journal of Earth Sciences, v. 98, p. 1655–1675.

Alt, J.C., 1994, A sulfur isotopic profile through the Troodos ophiolite, Cyprus: Primary composition and the effects of seawater hydrothermal alteration: Geochimica et Cosmochimica Acta, v. 58, p. 1825–1840.

Altunkaynak, Ş., 2007, Collision-driven slab breakoff magmatism in northwestern Anatolia, Turkey: Journal of Geology, v. 115, p. 63–82.

Altunkaynak, Ş., and Dilek, Y., 2006, Timing and nature of postcollisional volcanism in western Anatolia and geodynamic implications: Geological Society of America Special Papers, v. 409, p. 321–351.

Aminzadeh, B., Shahabpour, J., and Maghami, M., 2011, Variation of rhenium contents in molybdenites from the Sar Cheshmeh porphyry Cu-Mo deposit in Iran: Resource Geology, v. 61, p. 290–295.

Arslan, M., Temizel, I., Abdioğlu, E., Kolaylı, H., Yücel, C., Boztuğ, D., and Şen, C., 2013, $^{40}Ar$-$^{39}Ar$ dating, whole-rock and Sr-Nd-Pb isotope geochemistry of post-collisional Eocene volcanic rocks in the southern part of the eastern Pontides (NE Turkey): Implications for magma evolution in extension-induced origin: Contributions to Mineralogy and Petrology, v. 166, p. 113–142.

Ataman, G., 1972, L'âge radiométrique du massif granodioritique d'Orhaneli: Bulletin of the Geological Society of Turkey, v. 15, p. 125–130.

Bajwah, Z.U., Seccombe, P.K., and Offler, R., 1987, Trace element distribution, Co: Ni ratios and genesis of the Big Cadia iron-copper deposit, New South Wales, Australia: Mineralium Deposita, v. 22, p. 292–300.

Becker, H., and Dale, C.W., 2016, Re-Pt-Os isotopic and highly siderophile element behavior in oceanic and continental mantle tectonites: Reviews in Mineralogy and Geochemistry, v. 81, p. 369–440.

Bernard, A., Symonds, R.B., and Rose, W.I., 1990, Volatile transport and deposition of Mo, W and Re in high temperature magmatic fluids: Applied Geochemistry, v. 5, p. 317–326.

Berzina, A.N., Sotnikov, V.I., Economou-Eliopoulos, M., and Eliopoulos, D.G., 2005, Distribution of rhenium in molybdenite from porphyry Cu-Mo and Mo-Cu deposits of Russia (Siberia) and Mongolia: Ore Geology Reviews, v. 26, p. 91–113.

Bingöl, E., Delaloye, M., and Ataman, G., 1982, Granitic intrusions in western Anatolia: A contribution to the geodynamic study of this area: Eclogae Geologicae Helvetiae, v. 75, p. 437–446.

Bodnar, R.J., Lecumberri-Sanchez, P., Moncada, D., and Steele-MacInnis, M., 2013, Fluid inclusions in hydrothermal ore deposits, *in* Holland, H.D., and Turekian, K.K., eds., Treatise on geochemistry, 2nd ed.: Oxford, Elsevier Ltd., p. 119–142.

Bowen, G.J., and Wilkinson, B., 2002, Spatial distribution of $\delta^{18}O$ in meteoric precipitation: Geology, v. 30, p. 315–318.

Bowman, J.R., Parry, W.T., Kropp, W.P., and Kruer, S.A., 1987, Chemical and isotopic evolution of hydrothermal solutions at Bingham, Utah: Economic Geology, v. 82, p. 395–428.

Boztug, D., and Arehart, G.B., 2007, Oxygen and sulfur isotope geochemistry revealing a significant crustal signature in the genesis of the post-collisional granitoids in central Anatolia, Turkey: Journal of Asian Earth Sciences, v. 30, p. 403–416.

Boztuğ, D., and Harlavan, Y., 2008, K-Ar ages of granitoids unravel the stages of Neo-Tethyan convergence in the eastern Pontides and central Anatolia, Turkey: International Journal of Earth Sciences, v. 97, p. 585–599.

Boztuğ, D., Erçin, A.İ., Kuruçelik, M.K., Göç, D., Kömür, İ., and İskenderoğlu, A., 2006, Geochemical characteristics of the composite Kaçkar batholith generated in a Neo-Tethyan convergence system, eastern Pontides, Turkey: Journal of Asian Earth Sciences, v. 27, p. 286–302.

Bralia, A., Sabatini, G., and Troja, F., 1979, A revaluation of the Co/Ni ratio in pyrite as geochemical tool in ore genesis problems: Mineralium Deposita, v. 14, p. 353–374.

Chakhmouradian, A.R., Smith, M.P., and Kynicky, J., 2015, From "strategic" tungsten to "green" neodymium: A century of critical metals at a glance: Ore Geology Reviews, v. 64, p. 455–458.

Chaussidon, M., Albarède, F., and Sheppard, S.M.F., 1989, Sulphur isotope variations in the mantle from ion microprobe analyses of micro-sulphide inclusions: Earth and Planetary Science Letters, v. 92, p. 144–156.

Chouinard, A., Paquette, J., and Williams-Jones, A.E., 2005, Crystallographic controls on trace-element incorporation in auriferous pyrite from the Pascua epithermal high-sulfidation deposit, Chile-Argentina: Canadian Mineralogist, v. 43, p. 951–963.

Cioacă, M.E., Munteanu, M., Qi, L., and Costin, G., 2014, Trace element concentrations in porphyry copper deposits from Metaliferi Mountains, Romania: A reconnaissance study: Ore Geology Reviews, v. 63, p. 22–39.

Ciobanu, C.L., Cook, N.J., Kelson, C.R., Guerin, R., Kalleske, N., and Danyushevsky, L., 2013, Trace element heterogeneity in molybdenite fingerprints stages of mineralization: Chemical Geology, v. 347, p. 175–189.

Claypool, G.E., Holser, W.T., Kaplan, I.R., Sakai, H., and Zak, I., 1980, The age curves of sulfur and oxygen isotopes in marine sulfate and their mutual interpretation: Chemical Geology, v. 28, p. 199–260.

Clayton, R.N., O'Neil, J.R., and Mayeda, T.K., 1972, Oxygen isotope exchange between quartz and water: Journal of Geophysical Research, v. 77, p. 3057–3067.

Cloos, M., 2001, Bubbling magma chambers, cupolas, and porphyry copper deposits: International Geology Review, v. 43, p. 37–41.

Coleman, M.L., and Moore, M.P., 1978, Direct reduction of sulfates to sulfate dioxide for isotopic analysis: Analytical Chemistry, v. 50, p. 1594–1595.

Cook, N.J., Ciobanu, C.L., and Mao, J., 2009, Textural control on gold distribution in As-free pyrite from the Dongping, Huangtuliang and Hougou gold deposits, North China craton (Hebei Province, China): Chemical Geology, v. 264, p. 101–121.

Cook, N.J., Ciobanu, C.L., Meria, D., Silcock, D., and Wade, B., 2013, Arsenopyrite-pyrite association in an orogenic gold ore: Tracing mineralization history from textures and trace elements: Economic Geology, v. 108, p. 1273–1283.

Deditius, A.P., Utsunomiya, S., Reich, M., Kesler, S.E., Ewing, R.C., Hough, R., and Walshe, J., 2011, Trace metal nanoparticles in pyrite: Ore Geology Reviews, v. 42, p. 32–46.

Deditius, A.P., Reich, M., Kesler, S.E., Utsunomiya, S., Chryssoulis, S.L., Walshe, J., and Ewing, R.C., 2014, The coupled geochemistry of Au and As in pyrite from hydrothermal ore deposits: Geochimica et Cosmochimica Acta, v. 140, p. 644–670.

Delaloye, M., and Bingol, E., 2000, Granitoids from western and northwestern Anatolia: Geochemistry and modeling of geodynamic evolution: International Geology Review, v. 42, p. 241–268.

Dokuz, A., Karsli, O., Chen, B., and Uysal, İ., 2010, Sources and petrogenesis of Jurassic granitoids in the Yusufeli area, northeastern Turkey: Implications for pre-and post-collisional lithospheric thinning of the eastern Pontides: Tectonophysics, v. 480, p. 259–279.

Donnelly, T., Waldron, S., Tait, A., Dougans, J., and Bearhop, S., 2001, Hydrogen isotope analysis of natural abundance and deuterium-enriched waters by reduction over chromium on-line to a dynamic dual inlet isotope-ratio mass spectrometer: Rapid Communications in Mass Spectrometry, v. 15, p. 1297–1303.

Drábek, M., 1995, The Mo-Se-S and the Mo-Te-S systems: Neues Jahrbuch fur Mineralogie-Abhandlungen, v. 169, p. 255–263.

Eastoe, C.J., 1983, Sulfur isotope data and the nature of the hydrothermal systems at the Panguna and Frieda porphyry copper deposits, Papua New Guinea: Economic Geology, v. 78, p. 201–213.

Espurt, N., Hippolyte, J.-C., Kaymakci, N., and Sangu, E., 2014, Lithospheric structural control on inversion of the southern margin of the Black Sea Basin, central Pontides, Turkey: Lithosphere, v. 6, p. 26–34.

Fagerland, M.W., 2012, T-tests, non-parametric tests, and large studies—a paradox of statistical practice?: BMC Medical Research Methodology, v. 12, p. 78.

Fallick, A.E., McConville, P., Boyce, A.J., Burgess, R., and Kelley, S.P., 1992, Laser microprobe stable isotope measurements on geological materials: Some experimental considerations (with special reference to $\delta^{34}S$ in sulphides): Chemical Geology: Isotope Geoscience Section, v. 101, p. 53–61.

Fleischer, M., 1959, The geochemistry of rhenium, with special reference to its occurrence in molybdenite: Economic Geology, v. 54, p. 1406–1413.

Fonseca, R., Mallmann, G., O'Neill, H.S.C., and Campbell, I.H., 2007, How chalcophile is rhenium? An experimental study of the solubility of Re in sulphide mattes: Earth and Planetary Science Letters, v. 260, p. 537–548.

Ford, J.H., and Green, D.C., 1977, An oxygen-and hydrogen-isotope study of the Panguna porphyry-copper deposit, Bougainville: Journal of the Geological Society of Australia, v. 24, p. 63–80.

Giggenbach, W.F., 1992, Isotopic shifts in waters from geothermal and volcanic systems along convergent plate boundaries and their origin: Earth and Planetary Science Letters, v. 113, p. 495–510.

Gleeson, S.A., Roberts, S., Fallick, A.E., and Boyce, A.J., 2008, Micro-Fourier transform infrared (FT-IR) and δD value investigation of hydrothermal vein quartz: Interpretation of fluid inclusion δD values in hydrothermal systems: Geochimica et Cosmochimica Acta, v. 72, p. 4595–4606.

Grabezhev, A.I., 2007, Rhenium in ores of porphyry copper deposits in the Urals: Doklady Earth Sciences, v. 413, p. 265–268.

Grabezhev, A.I., and Voudouris, P.C., 2014, Rhenium distribution in molybdenite from the Vosnesensk porphyry Cu ± (Mo, Au) deposit (southern Urals, Russia): Canadian Mineralogist, v. 52, p. 671–686.

Harris, N.B.W., Pearce, J.A., and Tindle, A.G., 1986, Geochemical characteristics of collision-zone magmatism: Geological Society of London, Special Publications, v. 19, p. 67–81.

Hattori, K.H., and Keith, J.D., 2001, Contribution of mafic melt to porphyry copper mineralization: Evidence from Mount Pinatubo, Philippines, and Bingham Canyon, Utah, USA: Mineralium Deposita, v. 36, p. 799–806.

Huston, D.L., Sie, S.H., Suter, G.F., Cooke, D.R., and Both, R.A., 1995, Trace elements in sulfide minerals from eastern Australian volcanic-hosted massive sulfide deposits: Part I. Proton microprobe analyses of pyrite, chalcopyrite, and sphalerite, and Part II. Selenium levels in pyrite: Comparison with $\delta^{34}S$ values and implications for the source of sulfur in volcanogenic hydrothermal systems: Economic Geology, v. 90, p. 1167–1196.

Imai, N., Terashima, S., Itoh, S., and And, A., 1995, 1994 compilation of analytical data for minor and trace elements in seventeen reference "igneous series": Geostandards Newsletter, v. 19, p. 135–213.

Imbach, T., 1997, Deep groundwater circulation in the tectonically active area of Bursa, northwest Anatolia, Turkey: Geothermics, v. 26, p. 251–278.

Ito, K., and Kennedy, G.C., 1967, Melting and phase relations in a natural peridotite to 40 kilobars: American Journal of Science, v. 265, p. 519–538.

John, D., 2015, Rhenium—a rare metal critical to modern transportation: United States Geological Survey (USGS) Mineral Resources Program, p. 6–7.

Kajiwara, Y., and Krouse, H.R., 1971, Sulfur isotope partitioning in metallic sulfide systems: Canadian Journal of Earth Sciences, v. 8, p. 1397–1408.

Kaygusuz, A., Siebel, W., Şen, C., and Satir, M., 2008, Petrochemistry and petrology of I-type granitoids in an arc setting: The composite Torul pluton, eastern Pontides, NE Turkey: International Journal of Earth Sciences, v. 97, p. 739–764.

Kaymakci, N., Özçelik, Y., White, S.H., and Van Dijk, P.M., 2009, Tectonostratigraphy of the Çankırı Basin: Late Cretaceous to early Miocene evolution of the Neotethyan suture zone in Turkey: Geological Society of London, Special Publications, v. 311, p. 67–106.

Koptagel, O., Efe, A., Ulusoy, U., and Fallick, A.E., 1998, Sulfur-isotope study of the Ana Yatak massive sulfide deposit, southeastern Turkey: International Geology Review, v. 40, p. 363–374.

Kuscu, I., 2016, Magmatic evolution and metallogeny of Turkey [abs.]: Society of Economic Geologists, Maden Jeologları Derneği, Tethyan Tectonics and Metallogeny, SEG-MJD 2016 Conference, Çesme, Turkey, September 25–28, 2016, Abstracts, p. 1–2.

Lefebvre, C., Meijers, M.J.M., Kaymakci, N., Peynircioğlu, A., Langereis, C.G., and Van Hinsbergen, D.J.J., 2013, Reconstructing the geometry of central Anatolia during the Late Cretaceous: Large-scale Cenozoic rotations and deformation between the Pontides and Taurides: Earth and Planetary Science Letters, v. 366, p. 83–98.

Li, Y., and Liu, J., 2006, Calculation of sulfur isotope fractionation in sulfides: Geochimica et Cosmochimica Acta, v. 70, p. 1789–1795.

Mao, J., Du, A., Seltmann, R., and Yu, J., 2003, Re-Os ages for the Shameika porphyry Mo deposit and the Lipovy Log rare metal pegmatite, central Urals, Russia: Mineralium Deposita, v. 38, p. 251–257.

Matsuhisa, Y., Goldsmith, J.R., and Clayton, R.N., 1979, Oxygen isotopic fractionation in the system quartz-albite-anorthite-water: Geochimica et Cosmochimica Acta, v. 43, p. 1131–1140.

Naumov, A., 2007, Rhythms of rhenium: Russian Journal of Non-Ferrous Metals, v. 48, p. 418–423.

Newberry, R., 1979, Polytypism in molybdenite (II); relationships between polytypism, ore deposition/alteration stages and rhenium contents: American Mineralogist, v. 64, p. 768–775.

Oeser, M., Strauss, H., Wolff, P.E., Koepke, J., Peters, M., Garbe-Schönberg, D., and Dietrich, M., 2012, A profile of multiple sulfur isotopes through the Oman ophiolite: Chemical Geology, v. 312–313, p. 27–46.

Ohmoto, H., 1972, Systematics of sulfur and carbon isotopes in hydrothermal ore deposits: Economic Geology, v. 67, p. 551–578.

Ohmoto, H., and Rye, R., 1979, Isotopes of sulfur and carbon, *in* Barnes, H.L. ed., Geochemistry of hydrothermal deposits: Hoboken, New Jersey, John Wiley and Sons, p. 509–567.

Okay, A.I., 2008, Geology of Turkey: A synopsis: Anschnitt, v. 21, p. 19–42.

Okay, A.I., and Tüysüz, O., 1999, Tethyan sutures of northern Turkey: Geological Society of London, Special Publications, v. 156, p. 475–515.

Pašava, J., Vymazalová, A., Košler, J., Koneev, R.I., Jukov, A.V., and Khalmatov, R.A., 2010, Platinum-group elements in ores from the Kalmakyr porphyry Cu-Au-Mo deposit, Uzbekistan: Bulk geochemical and laser ablation ICP-MS data: Mineralium Deposita, v. 45, p. 411–418.

Pasava, J., Svojtka, M., Veselovský, F., Ďurišová, J., Ackerman, L., Pour, O., Drábek, M., Halodová, P., and Haluzová, E., 2016, Laser ablation ICPMS study of trace element chemistry in molybdenite coupled with scanning electron microscopy (SEM)—an important tool for identification of different types of mineralization: Ore Geology Reviews, v. 72, p. 874–895.

Patten, C., Barnes, S.J., Mathez, E.A., and Jenner, F.E., 2013, Partition coefficients of chalcophile elements between sulfide and silicate melts and the early crystallization history of sulfide liquid: LA-ICP-MS analysis of MORB sulfide droplets: Chemical Geology, v. 358, p. 170–188.

Peucker-Ehrenbrink, B., Hanghoj, K., Atwood, T., and Kelemen, P.B., 2012, Rhenium-osmium isotope systematics and platinum group element concentrations in oceanic crust: Geology, v. 40, p. 199–202.

Piercey, S.J., 2014, Modern analytical facilities 2. A review of quality assurance and quality control (QA/QC) procedures for lithogeochemical data: Geoscience Canada, v. 41, p. 75–88.

Polyak, D.E., 2016, Rhenium: USGS Mineral Commodity Summaries, p. 130–131.

Prichard, H.M., Knight, R.D., Fisher, P.C., McDonald, I., Zhou, M.F., and Wang, C.Y., 2013, Distribution of platinum-group elements in magmatic and altered ores in the Jinchuan intrusion, China: An example of selenium remobilization by postmagmatic fluids: Mineralium Deposita, v. 48, p. 767–786.

Rathkopf, C., Mazdab, F., Barton, I., and Barton, M.D., 2017, Grain-scale and deposit-scale heterogeneity of Re distribution in molybdenite at the Bagdad porphyry Cu-Mo deposit, Arizona: Journal of Geochemical Exploration, v. 178, p. 45–54.

Ravizza, G., Blusztajn, J., and Prichard, H.M., 2001, Re-Os systematics and platinum-group element distribution in metalliferous sediments from the Troodos ophiolite: Earth and Planetary Science Letters, v. 188, p. 369–381.

Reich, M., Kesler, S.E., Utsunomiya, S., Palenik, C.S., Chryssoulis, S.L., and Ewing, R.C., 2005, Solubility of gold in arsenian pyrite: Geochimica et Cosmochimica Acta, v. 69, p. 2781–2796.

Reich, M., Deditius, A., Chryssoulis, S., Li, J.W., Ma, C.Q., Parada, M.A., Barra, F., and Mittermayr, F., 2013, Pyrite as a record of hydrothermal fluid evolution in a porphyry copper system: A SIMS/EMPA trace element study: Geochimica et Cosmochimica Acta, v. 104, p. 42–62.

Richards, J.P., 2011, Magmatic to hydrothermal metal fluxes in convergent and collided margins: Ore Geology Reviews, v. 40, p. 1–26.

——2014, Porphyry and related deposits in subduction and post-subduction settings: Acta Geologica Sinica - English Edition, v. 88, p. 535–537.

Robertson, A.H.F., Parlak, O., and Ustaömer, T., 2009, Melange genesis and ophiolite emplacement related to subduction of the northern margin of the Tauride-Anatolide continent, central and western Turkey: Geological Society of London, Special Publications, v. 311, p. 9–66.

Robinson, B.W., and Kusakabe, M., 1975, Quantitative preparation of sulfur dioxide, for sulfur-34/sulfur-32 analyses, from sulfides by combustion with cuprous oxide: Analytical Chemistry, v. 47, p. 1179–1181.

Rye, R.O., 1993, SEG Distinguished Lecture: The evolution of magmatic fluids in the epithermal environment: The stable isotope perspective: Economic Geology, v. 88, p. 733–753.

——2005, A review of the stable-isotope geochemistry of sulfate minerals in selected igneous environments and related hydrothermal systems: Chemical Geology, v. 215, p. 5–36.

Sakınç, M., Yaltırak, C., and Oktay, F.Y., 1999, Palaeogeographical evolution of the Thrace Neogene Basin and the Tethys-Paratethys relations at northwestern Turkey (Thrace): Palaeogeography, Palaeoclimatology, Palaeoecology, v. 153, p. 17–40.

Sarıfakıoğlu, E., Özen, H., Çolakoğlu, A., and Sayak, H., 2010, Petrology, mineral chemistry, and tectonomagmatic evolution of Late Cretaceous suprasubduction-zone ophiolites in the İzmir-Ankara-Erzincan suture zone, Turkey: International Geology Review, v. 52, p. 187–222.

Sarıfakıoğlu, E., Dilek, Y., and Winchester, J.A., 2013, Late Cretaceous subduction initiation and Palaeocene-Eocene slab breakoff magmatism in south-central Anatolia, Turkey: International Geology Review, v. 55, p. 66–87.

Seal, R.R., 2006, Sulfur isotope geochemistry of sulfide minerals: Reviews in Mineralogy and Geochemistry, v. 61, p. 633–677.
Sharp, Z.D., 1990, A laser-based microanalytical method for the in situ determination of oxygen isotope ratios of silicates and oxides: Geochimica et Cosmochimica Acta, v. 54, p. 1353–1357.
Sheppard, S.M.F., and Gustafson, L.B., 1976, Oxygen and hydrogen isotopes in the porphyry copper deposit at El Salvador, Chile: Economic Geology, v. 71, p. 1549–1559.
Sheppard, S.M.F., Nielsen, R.L., and Taylor, H.P., Jr., 1971, Hydrogen and oxygen isotope ratios in minerals from porphyry copper deposits: Economic Geology, v. 66, p. 515–542.
Sillitoe, R.H., 2010, Porphyry copper systems: Economic Geology, v. 105, p. 3–41.
Sinclair, W.D., 2007, Porphyry deposits: Geological Association of Canada, Mineral Deposits Division, Special Publication 5, p. 223–243.
Sinclair, W.D., and Jonasson, I.R., 2014, Highly siderophile elements (Re, Au and PGE) in porphyry deposits and their mantle origins: Acta Geologica Sinica, v. 88, p. 616–618.
Singer, D.A., Berger, V I., Menzie, W.D., and Berger, B.R., 2005, Porphyry copper deposit density: Economic Geology, v. 100, p. 491–514.
Spencer, E.T., Wilkinson, J.J., Creaser, R.A., and Seguel, J., 2015, The distribution and timing of molybdenite mineralization at the El Teniente Cu-Mo porphyry deposit, Chile: Economic Geology, v. 110, p. 387–421.
Stein, H.J., Markey, R.J., Morgan, J.W., Selby, D., Creaser, R.A., McCuaig, T.C., and Behn, M., 2001a, Re-Os dating of Boddington molybdenite, SW Yilgarn: Two Au mineralization events: Australian Geological Survey Organisation (AGSO)-Geoscience Australia, Record, v. 37, p. 469–471.
Stein, H.J., Markey, R.J., Morgan, J.W., Hannah, J.L., and Scherstén, A., 2001b, The remarkable Re-Os chronometer in molybdenite: How and why it works: Terra Nova, v. 13, p. 479–486.
Stratex International, 2011, Maiden resource for Muratdere porphyry copper-gold project, Turkey: Interim Report and Accounts, www.investegate.co.uk/stratex-int-plc--orr-/rns/maiden-resource-for-muratdere--turkey/201106150700104424I/, 7 p.
——2017, Annual report 2017, www.stratexinternational.com/wp-content/uploads/2018/03/Stratex-Annual-Report-2017.pdf, 56 p.
Sun, W., Arculus, R.J., Bennett, V.C., Eggins, S.M., and Binns, R.A., 2003, Evidence for rhenium enrichment in the mantle wedge from submarine arc-like volcanic glasses (Papua New Guinea): Geology, v. 31, p. 845–848.
Sykora, S., Cooke, D.R., Meffre, S., Stephanov, A.S., Gardner, K., Scott, R., Selley, D., and Harris, A.C., 2018, Evolution of pyrite trace element compositions from porphyry-style and epithermal conditions at the Lihir gold deposit: Implications for ore genesis and mineral processing: Economic Geology, v. 113, p. 193–208.
Taylor, H.P., and Sheppard, S.M.F., 1986, Igneous rocks; I, Processes of isotopic fractionation and isotope systematics: Reviews in Mineralogy and Geochemistry, v. 16, p. 227–271.
Tekeli, O., 1981, Subduction complex of pre-Jurassic age, northern Anatolia, Turkey: Geology, v. 9, p. 68–72.
Tessalina, S.G., Yudovskaya, M.A., Chaplygin, I.V, Birck, J.L., and Capmas, F., 2008, Sources of unique rhenium enrichment in fumaroles and sulphides at Kudryavy volcano: Geochimica et Cosmochimica Acta, v. 72, p. 889–909.
Thode, H.G., and Monster, J., 1965, Sulfur-isotope geochemistry of petroleum, evaporites, and ancient seas: American Association of Petroleum Geologists (AAPG) Special Publications, Memoir 4, p. 367–377.
Uysal, I., Zaccarini, F., Sadiklar, M.B., Tarkian, M., Thalhammer, O.A.R., and Garuti, G., 2009, The podiform chromitites in the Dagküplü and Kavad mines, Eskisehir ophiolite (NW-Turkey): Genetic implications of mineralogical and geochemical data: Geologica Acta, v. 7, p. 351–362.
Voudouris, P., 2006, A comparative mineralogical study of Te-rich magmatic-hydrothermal systems in northeastern Greece: Mineralogy and Petrology, v. 87, p. 241–275.
Voudouris, P.C., Melfos, V., Spry, P.G., Bindi, L., Kartal, T., Arikas, K., Moritz, R., and Ortelli, M., 2009, Rhenium-rich molybdenite and rheniite in the Pagoni Rachi Mo-Cu-Te-Ag-Au prospect, northern Greece: Implications for the Re geochemistry of porphyry-style Cu-Mo and Mo mineralization: Canadian Mineralogist, v. 47, p. 1013–1036.
Wagner, T., Boyce, A.J., and Fallick, A.E., 2002, Laser combustion analysis of $\delta^{34}S$ of sulfosalt minerals: Geochimica et Cosmochimica Acta, v. 66, p. 2855–2863.
Wilson, A.J., Cooke, D.R., Stein, H.J., Fanning, C.M., Holliday, J.R., and Tedder, I.J., 2007, U-Pb and Re-Os geochronologic evidence for two alkalic porphyry ore-forming events in the Cadia district, New South Wales, Australia: Economic Geology, v. 102, p. 3–26.
Winderbaum, L., Ciobanu, C.L., Cook, N.J., Paul, M., Metcalfe, A., and Gilbert, S., 2012, Multivariate analysis of an LA-ICP-MS trace element dataset for pyrite: Mathematical Geosciences, v. 44, p. 823–842.
Xiong, Y., and Wood, S.A., 2002, Experimental determination of the hydrothermal solubility of $ReS_2$ and the Re-$ReO_2$ buffer assemblage and transport of rhenium under supercritical conditions: Geochemical Transactions, v. 3, p. 1.
Xiong, Y., Wood, S., and Kruszewski, J., 2006, Hydrothermal transport and deposition of rhenium under subcritical conditions revisited: Economic Geology, v. 101, p. 471–478.
Yigit, O., 2006, Gold in Turkey—a missing link in Tethyan metallogeny: Ore Geology Reviews, v. 28, p. 147–179.
——2009, Mineral deposits of Turkey in relation to Tethyan metallogeny: Implications for future mineral exploration: Economic Geology, v. 104, p. 19–51.
Zaluski, G., Nesbitt, B., and Muehlenbachs, K., 1994, Hydrothermal alteration and stable isotope systematics of the Babine porphyry Cu deposits, British Columbia; implications for fluid evolution of porphyry systems: Economic Geology, v. 89, p. 1518–1541.
Zarasvandi, A., Rezaei, M., Raith, J.G., Pourkaseb, H., Asadi, S., Saed, M., and Lentz, D.R., 2018, Metal endowment reflected in chemical composition of silicates and sulfides of mineralized porphyry copper systems, Urumieh-Dokhtar magmatic arc, Iran: Geochimica et Cosmochimica Acta, v. 223, p. 36–59.
Zhang, P., Huang, X.-W., Cui, B., Wang, B.-C., Yin, Y.-F., and Wang, J.-R., 2016, Re-Os isotopic and trace element compositions of pyrite and origin of the Cretaceous Jinchang porphyry Cu-Au deposit, Heilongjiang Province, NE China: Journal of Asian Earth Sciences, v. 129, p. 67–80.

**Katie McFall** is a geologist and geochemist who specializes in magmatic and magmatic-hydrothermal mineral deposits. She is currently a postdoctoral research associate at Cardiff University, UK, working on the Cycling and Supply of Te and Se (TeaSe) consortium, part of the NERC Security of Supply minerals program. Katie received her M.Sci. and Ph.D. (2016) degrees from the University of Southampton, UK. She works on porphyry Cu deposits and magmatic sulfide deposits, applying a wide variety of techniques to understand ore deposit formation and the behavior of chalcophile and critical elements in magmatic-hydrothermal systems.